

# Constraining the structure of the transition disk HD 135344B (SAO 206462) by simultaneous modeling of multi-wavelength gas and dust observations <sup>★, ★★</sup>

A. Carmona<sup>1</sup>, C. Pinte<sup>2,1</sup>, W.F. Thi<sup>1</sup>, M. Benisty<sup>1</sup>, F. Ménard<sup>2,1</sup>, C. Grady<sup>3,4,5</sup>, I. Kamp<sup>6</sup>, P. Woitke<sup>7</sup>, J. Olofsson<sup>8</sup>, A. Roberge<sup>5</sup>, S. Brittain<sup>9</sup>, G. Dûchene<sup>10,1</sup>, G. Meeus<sup>11</sup>, C. Martin-Zaïdi<sup>1</sup>, B. Dent<sup>12</sup>, J.B. Le Bouquin<sup>1</sup>, J.P. Berger<sup>13,1</sup>

<sup>1</sup> UJF-Grenoble 1 / CNRS-INSU, Institut de Planétologie et d'Astrophysique de Grenoble (IPAG) UMR 5274, Grenoble, F-38041, France, e-mail: andres.carmona@obs.ujf-grenoble.fr

<sup>2</sup> UMI-FCA, CNRS / INSU France (UMI 3386), and Departamento de Astronomía, Universidad de Chile, Santiago, Chile

<sup>3</sup> Eureka Scientific, 2452 Delmer, Suite 100, Oakland CA 96002, USA

<sup>4</sup> ExoPlanets and Stellar Astrophysics Laboratory, Code 667, Goddard Space Flight Center, Greenbelt, MD 20771, USA

<sup>5</sup> Goddard Center for Astrobiology, Goddard Space Flight Center, Greenbelt, MD 20771, USA

<sup>6</sup> Kapteyn Astronomical Institute, P.O. Box 800, 9700 AV Groningen, The Netherlands

<sup>7</sup> SUPA, School of Physics and Astronomy, University of St Andrews, KY16 9SS, UK

<sup>8</sup> Max Planck Institut für Astronomie, Königstuhl 17, D-69117 Heidelberg, Germany

<sup>9</sup> Department of Physics & Astronomy, 118 Kinard Laboratory, Clemson University, Clemson, SC 29634, USA

<sup>10</sup> Astronomy Department, University of California, Berkeley, CA 94720-3411, USA

<sup>11</sup> Departamento de Física Teórica, Universidad Autónoma de Madrid, Campus Cantoblanco, Spain

<sup>12</sup> Joint ALMA Observatory, Alonso de Córdova 3107, Vitacura 763-0355, Santiago, Chile

<sup>13</sup> European Southern Observatory, Alonso de Córdova, 3107 Vitacura, Chile

Received 25 August 2013; accepted 23 March 2014

## ABSTRACT

**Context.** Constraining the gas and dust disk structure of transition disks, particularly in the inner dust cavity, is a crucial step towards understanding the link between them and planet formation. HD 135344B is an accreting (pre-) transition disk which displays emission of warm CO extending tens of AU inside its 30 AU dust cavity.

**Aims.** We constrain HD 135344B's disk structure from multi-instrument gas and dust observations.

**Methods.** We employ the dust radiative transfer code MCFOST and the thermo-chemical code ProDiMo to derive the disk structure from the simultaneous modeling of the spectral energy distribution (SED), VLT/CRIRES CO P(10) 4.75  $\mu$ m, Herschel/PACS [O I] 63  $\mu$ m, Spitzer-IRS, and JCMT <sup>12</sup>CO J=3-2 spectra, VLTI/PIONIER H-band visibilities, and constraints from (sub-)mm continuum interferometry and near-IR imaging.

**Results.** We found a disk model able to describe simultaneously the current gas and dust observations. This disk has the following structure: (1) to reproduce simultaneously the SED, the near-IR interferometry data, and the CO ro-vibrational emission, refractory grains (we suggest carbon) are present inside the silicate sublimation radius ( $0.08 < R < 0.2$  AU); (2) the dust cavity ( $R < 30$  AU) is filled with gas, the surface density of the gas inside the cavity must increase with radius to fit the CO ro-vibrational line profile, a small gap of a few AU in the gas distribution is compatible with current data, a large gap of tens of AU in the gas appears not likely; (4) the gas-to-dust ratio inside the cavity is  $> 100$  to account for the 870  $\mu$ m continuum upper limit and the CO P(10) line flux; (5) the gas-to-dust ratio in the outer disk ( $30 < R < 200$  AU) is  $< 10$  to simultaneously describe the [O I] 63  $\mu$ m line flux and the CO P(10) line profile; (6) in the outer disk most of the gas and dust mass should be located in the mid-plane and a significant fraction of the dust should be in large grains.

**Conclusions.** Simultaneous modeling of the gas and dust it is required to break the model degeneracies and constrain the disk structure. An increasing gas surface density with radius in the inner cavity echoes the effect of a migrating jovian planet in the disk structure. The global low gas mass (a few Jupiter masses) in the HD 135344B's disk supports the idea that it is an evolved disk that has already lost a large fraction of its mass.

**Key words.** protoplanetary disks – stars: individual: HD 135344B (SAO 206462), pre-main sequence – planets and satellites: formation – techniques: imaging, spectroscopy, interferometric.

## 1. Introduction

Observations of young stars of different ages reveal that protoplanetary disks evolve from optically thick gas-rich disks to optically thin gas-poor debris-disks (e.g. see review by Williams & Cieza 2011). The transition between these two classes of objects is believed to occur relatively fast ( $10^5$  years) compared to the disk's life time (5 - 10 Myr) (e.g., Cieza et al. 2007; Damjanov et al. 2007; Currie & Sicilia-Aguilar 2011). Infrared space ob-

\* Based on PIONIER, CRIRES, and UVES observations collected at the VLTI and VLT (European Southern Observatory, Paranal, Chile) with programs 087.C-0702(A,B,D), 087.C-0458(C), 087.C-0703(B), 179.C-0151(A), 077.C-0521(A)

\*\* *Herschel* is an ESA space observatory with science instruments provided by European-led Principal Investigator consortia and with important participation from NASA.

servatories have unveiled several young stars with spectral energy distributions (SED) characterized by IR-excess at  $> 10 \mu\text{m}$  and significantly reduced excesses at shorter wavelengths (e.g., Strom et al. 1989; Calvet et al. 2005; Sicilia-Aguilar et al. 2006; Hernández et al. 2006; Espaillat et al. 2007; Fang et al. 2009; Merín et al. 2010; Rebull et al. 2010; Cieza et al. 2010). These sources are commonly named “transition disks”, as they are believed to be the objects in the transition phase between a young star with an optically thick gas-rich disk and a star with an optically thin gas-poor debris disk.

Generally, the lack of strong emission in the near or mid-IR SED is interpreted as evidence for a gap or cavity from a few up to tens of AU in the disk. Follow-up imaging of several transition disks with sub-mm interferometers have confirmed that transition disks indeed have a deficit of sub-mm continuum emission at a few mJy levels inside tens of AU (e.g., Piétu et al. 2007; Brown et al. 2009; Hughes et al. 2009; Andrews et al. 2011; Isella et al. 2012), thus providing further evidence for such inner disk cavities, at least on the large dust grains.

Several scenarios are discussed in the literature to explain the presence of a cavity and the transitional disk SED shape: grain-growth (e.g., Dullemond & Dominik 2005; Birnstiel et al. 2012), migrating giant planets that opened a gap (e.g., Varnière et al. 2006; Zhu et al. 2011; Dodson-Robinson & Salyk 2011), dust filtration by a giant planet (e.g., Rice et al. 2006; Zhu et al. 2012; Pinilla et al. 2012), disk dissipation due to a photoevaporative disk wind (e.g., Alexander & Armitage 2007; Owen et al. 2012), and dust free inner holes due to radiation pressure (Chiang & Murray-Clay 2007). One important step to understand the transitional disk phenomenon is to understand how the gas and dust structures compare. Do they follow each other in density structure? do they thermally de-couple? does the gas-to-dust ratio stay constant as a function of the radius?

Several young stars with transition disks are emission line-stars that exhibit signs of accretion (e.g., Najita et al. 2007b; Muzerolle et al. 2010; Cieza et al. 2012). As a consequence, the cavities imaged in the sub-mm should have gas as the material from the optically thick outer disk flows through the cavity to be accreted by the central object (e.g., Lubow & D’Angelo 2006). In fact, several transition disks display emission of CO at  $4.7 \mu\text{m}$  (e.g., Salyk et al. 2009) a common tracer of warm gas in the inner disk (e.g. Najita et al. 2007a). Furthermore, in a few transition disks CO ro-vibrational emission has been spatially resolved up to distances of tens of AU (Pontoppidan et al. 2008). Moreover, recent studies of dust scattered light in the near-IR have detected emission from small dust inside the cavities that were previously imaged with sub-mm interferometry, with the additional and remarkable property that no sharp edge is seen at the location of the sub-mm cavity inner-radius (e.g. Muto et al. 2012; Garufi et al. 2013). This is suggesting that what is observed is likely a change in the dust size distribution inside the cavity (Dong et al. 2012). Near-IR interferometry provides evidence for dust emission (and inhomogeneities) inside the dust cavity of transition disks (e.g. Kraus et al. 2013). Furthermore, recent ALMA observations have spatially resolved gas inside the cavity of transition disks (Casassus et al. 2013; Bruderer et al. 2013).

In summary, the observational evidence indicating that the dust cavities of transitions disks are indeed *not empty* has been steadily growing during the last years. This opens interesting questions such as: how much gas and dust are present in these cavities? how are they distributed? what is their chemical composition? if dust is present, what is its size distribution? if there is gap in the gas or the dust how large is it?

The goal of this paper is to address the problem of the gas and dust structure in transition disks, by performing a detailed study of the transition disk HD 135344B (SAO 206462). Our aim is to constrain the disk structure by modeling simultaneously and in a coherent way multi-wavelength & multi-instrument gas and dust observations of the inner and the outer disk. Most specifically, we search to investigate gas and dust disk content and structure inside the cavity by modeling simultaneously the SED, new VLTI-PIONIER near-IR interferometry data, the CO  $4.7 \mu\text{m}$  emission, and constraints from sub-mm continuum interferometry. Furthermore, we seek to constrain the gas mass and the gas-to-dust ratio in the outer disk employing the SED, the [O I]  $63 \mu\text{m}$  and  $145 \mu\text{m}$  lines, and (sub-)mm observations.

HD 135344B is an accreting ( $2 \times 10^{-8} M_{\odot}/\text{yr}$ , Sitko et al. 2012) F4V young star ( $8^{+8}_{-4}$  Myr, van Boekel et al. 2005) which has a “pre-transition” disk (i.e., a transition disk with near-IR excess). It has the remarkable characteristic of exhibiting CO  $4.7 \mu\text{m}$  emission extending tens of AU inside the 45 AU sub-mm dust cavity (Pontoppidan et al. 2008) and scattered light emission from small dust down to 28 AU (Muto et al. 2012; Garufi et al. 2013). HD 135344B display spiral structures (Muto et al. 2012; Garufi et al. 2013) and asymmetries in its outer disk dust emission (Brown et al. 2009; Andrews et al. 2011). It is a transition disk exhibiting variability in its near-IR SED, and in optical and near-IR line emission in time scales of months (Sitko et al. 2012). It is a source on which [O I]  $63 \mu\text{m}$  emission has been detected in Herschel/PACS observations (Meeus et al. 2012). Finally, it is a transition disk without close-in low-mass stellar companions (Vicente et al. 2011).

We start the paper by a brief summary of current observational constraints on the disk of HD 135344B in Section 2. Then, in Section 3, we describe the modeling tools and the general modeling procedure. In Section 4, we present and discuss the different models that were tested. In Section 5, we examine the disk constraints derived from the final disk model. In Section 6, we discuss our results in the context of the study of transitional disks and planet formation. Finally a summary and conclusions are presented in Section 7.

## 2. Observational constraints

HD 135344B has been observed with a diversity of instruments and techniques from UV to mm wavelengths. In Table 1, we present a concise summary of relevant previous observational constraints on HD 135344B. The most important observational constraints for this study are:

- SED dip in the  $10\text{--}50 \mu\text{m}$  region (Brown et al. 2007);
- the  $10 \mu\text{m}$  silicate feature is absent (Geers et al. 2006);
- the inner radius of the sub-mm cavity is  $46 \pm 5$  AU (Brown et al. 2009; Andrews et al. 2011);
- $3\sigma$  continuum flux upper limit at  $870 \mu\text{m}$  for a  $0.24'' \times 0.5''$  beam centered on the star 10.5 mJy (Andrews et al. 2011);
- CO ro-vibrational emission extends at least to 15 AU inside the sub-mm dust cavity (25 AU for  $d=140$  pc) (Pontoppidan et al. 2008)<sup>1</sup>;
- near-IR dust scattering images reveal small dust inside the sub-mm cavity down to 28 AU with a smooth surface brightness and no discontinuity at 45 AU (Muto et al. 2012; Garufi et al. 2013).

<sup>1</sup> Pontoppidan et al. (2008) suggested a minimum extension of 15 AU assuming a distance of 84 pc. The distance currently used to interpret HD 135344B data (Brown et al. 2009; Andrews et al. 2011) is 140 pc (van Boekel et al. 2005). If  $R_{\text{out}}$  constraint is scaled to the 140 pc that leads to a minimum outer radius of 25 AU.

**Table 1.** Summary of most relevant previous observations and disk constraints.

Technique	Instrument	Observation	Interpretation or Constraint	Ref.
UV - mm photometry	several	SED: dip at 15 $\mu\text{m}$	40 AU gap	1,2
UV spectroscopy	HST-COS	shape of the continuum flux	Spectral Type F4V; E(B-V) < 0.129	3,4,5
optical spectroscopy	VLT-UVES	photospheric absorption lines	$T_{\text{eff}}=6750\pm250$ K; $\log g > 4.0$	this work
	VLT-UVES	broad [O I] 6300 Å emission	hot gas down to 0.1 AU	6,7
near-IR high-resolution spectroscopy	VLT-CRIRES	extended CO 4.7 $\mu\text{m}$ emission; line profile and spectroastrometry signal	gas in keplerian rotation inside the cavity at least until 15 AU assuming $d=84$ pc (25 AU @ 140 pc); $i=14^\circ$ for $M=1.65 M_\odot$ ; PA $\sim 56^\circ$	8
	VLT-CRIRES	non detection of H <sub>2</sub> lines at 2 $\mu\text{m}$	fluxes < $10^{-17}$ W m <sup>-2</sup>	9
near-IR imaging	Subaru-HICIAO	dust scattered light emission	material down to 28 AU; no discontinuity at 45 AU; spiral patterns; flat outer disk	10
	VLT-NACO		strong drop of polarized dust emission at 28 AU	11
near-IR interferometry	VLT/PIONIER	visibilities	continuum emission inside the silicate sublimation radius ( $R < 0.2$ AU)	this work
mid-IR spectroscopy	Spitzer/IRS	no 10 $\mu\text{m}$ silicate feature	limit to the mass of small silicate grains	12
		weak 11.2 $\mu\text{m}$ PAH emission	limit to the PAH abundance	13
far-IR spectroscopy	Herschel/PACS	non detection H <sub>2</sub> pure-rotational lines, and the [Ne II] 12.8 $\mu\text{m}$ line	fluxes < $10^{-17}$ W m <sup>-2</sup>	13
		[O I] 63 $\mu\text{m}$ detected, upper limits to the [O I] 145 $\mu\text{m}$ and [C II] 157 $\mu\text{m}$ lines	$F_{[\text{O I}] 63 \mu\text{m}}=3.6-4.8\times10^{-17}$ W m <sup>-2</sup>	14, 20
sub-mm interferometry	SMA	weak 870 $\mu\text{m}$ continuum at $R < 40$ AU;	cavity radius $46\pm5$ AU; $i \sim 12^\circ$ ; $3\sigma$ flux in a $0.24'' \times 0.5''$ ( $33 \times 70$ AU) beam centered on the star 10.5 mJy	15, 16
	ALMA	resolved 450 $\mu\text{m}$ emission <sup>12</sup> CO 6-5 detected at $R < 40$ AU	asymmetries in the outer disk observed gas inside the dust cavity.	17
sub-mm line single dish	JCMT	<sup>12</sup> CO 3-2 detected	double peak; $\text{FWHM}=2.2$ km/s; $i \sim 11^\circ$	18
mm continuum and line interferometry	SMA	extended 1.3 mm emission extended <sup>12</sup> CO 2-1 emission	$R_{\text{out}} = 220$ AU; $i \sim 11^\circ$	19

**References** [1] see Table A.1 in the Appendix, [2] Brown et al. (2007), [3] Grady et al. (2009), [4] France et al. (2012), [5] Schindhelm et al. (2012), [6] van der Plas et al. (2008), [7] Fedele et al. (2008), [8] Pontoppidan et al. (2008), [9] Carmona et al. (2011) [10] Muto et al. (2012), [11] Garufi et al. (2013), [12] Geers et al. (2006), [13] Lahuis et al. (2007), [14] Meeus et al. (2012), [15] Brown et al. (2009), [16] Andrews et al. (2011), [17] Perez et al. (2014, in prep), [18] Dent et al. (2005), [19] Lyo et al. (2011), [20] Fedele et al. (2013).

### 3. Modeling

#### 3.1. Stellar parameters

We provide a detailed discussion of the derivation of the stellar parameters in the Appendix A.2. For our models we used a star with  $T_{\text{eff}}=6620$  K (F4V), a stellar radius of  $2.1 R_\odot$ , a mass of  $1.65 M_\odot$ , and  $A_V = 0.4$ . Note that due to uncertainties in the photometry, the spectral type, and, specially, the distance ( $\pm 20$  pc) the stellar radius can vary  $\pm 0.3 R_\odot$  and the stellar mass  $\pm 0.1 M_\odot$ . The stellar UV spectrum<sup>2</sup> was parametrized with a fractional UV excess  $f_{\text{UV}} = L_{\text{UV}}/L_\star$  equal to 0.001 ( $L_{\text{UV}}$  is defined as the luminosity between 91.2 and 250 nm) and  $F_\nu \propto \nu^\gamma$  with  $\gamma = -2.15$ . This parametrized stellar UV spectrum is included in the ProDiMo gas heating calculation in addition to the interstellar UV field.

<sup>2</sup> FUSE and HST-COS spectra were obtained from DIANA protoplanetary disk observations and modeling database (<http://www.diana-project.com/>). Details on the data reduction procedures will be given in Dionatos et al. (in prep.).

#### 3.2. Disk inclination and position angle

Several data sets give different inclinations for HD 135344B: CO 4.7  $\mu\text{m}$  emission suggests  $i = 14^\circ \pm 4^\circ$  (Pontoppidan et al. 2008, for  $M = 1.65 M_\odot$ ); the CO  $J = 3 - 2$  line at 870  $\mu\text{m}$  indicates  $i = 11^\circ \pm 2^\circ$  (Dent et al. 2005); sub-mm continuum imaging points towards  $i = 12^\circ$  (Andrews et al. 2011) and  $21^\circ$  (Brown et al. 2009); mm interferometry suggests  $i = 11^\circ$  (Lyo et al. 2011); near-IR imaging sets an upper limit of  $i = 20^\circ$  Grady et al. (2009); mid-IR imaging suggests  $i = 46^\circ \pm 5^\circ$  (Doucet et al. 2006) and  $45^\circ \pm 5^\circ$  (Mariñas et al. 2011). For our analysis of the SED and line profiles we used  $i = 14^\circ$ . We used this value because it is derived from a simultaneous fit to the spectroastrometry signature of the CO 4.7  $\mu\text{m}$  line in 3 slit position angles and the spectrally resolved CO 4.7  $\mu\text{m}$  line profile, and because it is consistent with the inclination derived from the observations of CO gas in the outer disk<sup>3</sup>.

<sup>3</sup> Recent near-IR imaging (Muto et al. 2012; Garufi et al. 2013) and sub-mm interferometry (Brown et al. 2009, Perez et al. in prep) have revealed that the disk of HD 135344B has spiral arms and asymmetries in the dust emission. One possible reason for the discrepancy between the inclination derived from mid-IR imaging data (i.e. dust emission) and the inclination derived from near-IR and sub-mm CO gas observations

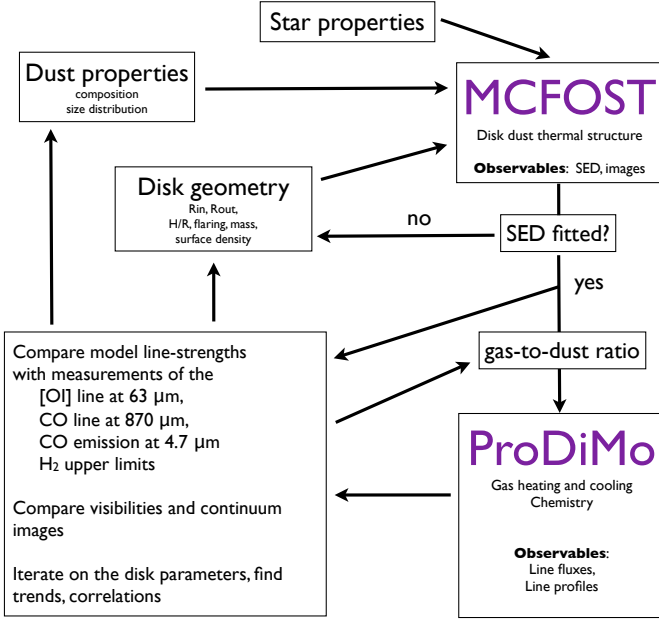


**Fig. 1.** Schematic view of the general modeling procedure.

Several estimations exist for the disk’s position angle (PA). Pontoppidan et al. (2008) suggest a  $PA=56^\circ \pm 2^\circ$  based on spectroastrometry of the CO  $4.7 \mu\text{m}$  emission; Grady et al. (2009) suggest a  $PA=55^\circ \pm 5^\circ$  based on near-IR scattered light imaging; Andrews et al. (2011), Brown et al. (2009), and Lyo et al. (2011) based on (sub-)mm interferometry continuum observations suggest a  $PA=64^\circ$ ,  $55^\circ$ , and  $64^\circ$  respectively. As we aim to compare our model with the CO  $4.7 \mu\text{m}$  lines we employed a PA of  $56^\circ$ .

### 3.3. Description of the general modeling procedure

We aimed to

1. *simultaneously fit* the SED, the line profile of the CO  $\nu = 1 - 0$  P(10) line at  $4.7545 \mu\text{m}$ , and the near-IR PIONIER visibilities and closure phases.
2. *reproduce within a factor of a few* the detected line fluxes of CO P(10), [O I] at  $63 \mu\text{m}$ ,  $^{12}\text{CO } J = 3 - 2$  at  $870 \mu\text{m}$ , and  $^{12}\text{CO } J = 2 - 1$  at  $1.27 \text{ mm}$ .
3. *obtain line fluxes below the upper limits* for [O I] at  $145 \mu\text{m}$ , [C II] at  $157 \mu\text{m}$ ,  $\text{H}_2 1 - 0 \text{ S}(1)$  at  $2.12 \mu\text{m}$ ,  $\text{H}_2 0 - 0 \text{ S}(1)$  at  $17 \mu\text{m}$ , and CO and  $\text{H}_2\text{O}$  infrared lines covered by Herschel (see Tables A.2 and A.3).
4. *obtain* a  $870 \mu\text{m}$  flux inside a beam of  $4'' \times 0.5''$  ( $33 \times 70 \text{ AU}$ ) centered on the star lower than  $10.5 \text{ mJy}$ .

To be consistent with the sub-mm continuum constraints, the inner radius of the outer disk’s large and small grains was set to  $45 \text{ AU}$ . Later in the modeling process, to be consistent with the near-IR scattered-light constraints, the inner radius of the outer disk’s small grains was allowed to extend down to  $30 \text{ AU}$ .

In Fig. 1, we provide an schematic overview of the modeling procedure. The modeling starts by assuming a dust composition, dust size distribution, dust mass, gas-to-dust ratio, for the inner and the outer disk using a parametric disk (see details in next section). Then the Monte-Carlo dust radiative transfer code

is that disk asymmetries could be present in the mid-IR dust emission, thus a different estimate of the inclination and PA.

MCFOST (Pinte et al. 2006, 2009) is used to calculate the dust thermal and density structure,  $T_{\text{dust}}(r, z)$ ,  $n_{\text{dust}}(r, z)$ , and the mean radiation field  $J_\nu(r, z)$ . MCFOST is employed to compute a synthetic SED, and continuum images in the H band and at  $870 \mu\text{m}$  for comparison with VLT/PIONIER and SMA continuum observations.

The MCFOST disk structure and radiation field is then employed as an input for the thermo-chemical radiative transfer code ProDiMo (Woitke et al. 2009). ProDiMo calculates the disk chemistry, the gas and dust heating and cooling, the energy level populations of molecules and atoms, and, using escape probability, ProDiMo computes the synthetic line fluxes and channel maps for gas emission lines from the optical to the mm.

Details of the coupling between the codes MCFOST and ProDiMo, and brief summaries of technical details of both codes are provided in Woitke et al. (2010), Pinte et al. (2010), and Kamp et al. (2011). Details of the implementation of CO ro-vibrational emission within ProDiMo are given in Thi et al. (2013).

The modeling was performed without computing the hydrostatic equilibrium, the disk gas and dust density distribution (thus the gas-to-dust ratio) was set as input so an iterative scheme between MCFOST and ProDiMo was used. We chose this approach to be able to explore a large fraction of the parameter space. Computing the hydrostatic equilibrium would have resulted in running time an order of magnitude longer and would have prevented us from performing such an exploration of the parameter space. We have verified that our last model, Model 5, is consistent with hydrostatic equilibrium: i.e. the scale height we used as input is consistent with  $h_{\text{hydro}} =$

$$\sqrt{kT_{\text{gas}}(z=0) r^3 / GM\mu}.$$

We started our exploration with simple models and complexity in the model was only added when we were not able to fit some of the observations. The model was refined sequentially following this protocol

1. fit the SED
2. fit the CO P(10) ro-vibrational line-profile
3. check consistency with SMA  $870 \mu\text{m}$  continuum upper limits inside the cavity
4. describe near-IR visibilities
5. produce an [O I]  $63 \mu\text{m}$  line flux consistent with the Herschel observations
6. refine the model to account for the latest near-IR polarization images (Garufi et al. 2013)

For each family of models, a large fraction of the parameter space was explored by a combination of hand exploration, grid modeling, and simplex optimization algorithms. In total we have tested around  $\sim 60\,000$  MCFOST models and  $\sim 4\,000$  ProDiMo models.

### 3.4. Disk structure & MCFOST parameters

The philosophy of MCFOST is to model the disk as composed of individual zones that may overlap. Each zone is a disk extending from an inner radius  $R_{\text{in}}$  to an outer radius  $R_{\text{out}}$ , with a scale height  $h_0$  at a reference radius  $r_0$ , flaring exponent ( $\beta$ ), surface density exponent ( $q$ ). Each zone has a Gaussian vertical density profile  $\rho(r, z) = \rho_0(r) \exp(-z^2/2h(r)^2)$ , a power-law surface density  $\Sigma(r) = \Sigma_0(r/r_0)^q$ , and a scale height  $h(r) = h_0(r/r_0)^\beta$ , where  $\beta$  is the flaring exponent,  $r$  is the radial coordinate in the equatorial plane, and  $h_0$  the scale height at the reference radius  $r_0$ .



**Table 2.** HD 135344B stellar and geometrical parameters used for the modeling.

$T_{\text{eff}}$	=	6620 K
$\log g$	=	4.5
$R$	=	2.1 $R_{\odot}$
$M$	=	1.65 $M_{\odot}$
$A_V$	=	0.4
$d$	=	140 pc
$i$	=	14°
$PA$	=	56°
$R_{\text{cav}}$	=	30–45 AU
$R_{\text{out}}$	=	200 AU

**Table 3.** ProDiMo general parameters.

ISM UV field ( $\chi$ , Draine)	=	1.0
Non-thermal broadening	=	0.15 km s <sup>-1</sup>
fractional UV excess	=	0.001
UV power-law index	=	-2.15
Cosmic ray ionization rate of H <sub>2</sub> $\zeta$	=	5×10 <sup>-17</sup> s <sup>-1</sup>

For each zone the dust composition, dust size distribution, dust mass, and gas-to-dust ratio are defined independently. One zone can include several dust components, for example silicate grains, carbonaceous grains or PAHs. Zones can have gaussian inner edges of size 5 times the parameter “*edge*”. In our models, for each zone, the gas-to-dust ratio is constant in the vertical direction.

Dust grains are defined as homogeneous and spherical particles with sizes distributed according to the power-law  $dn(a) \propto a^p da$ , with  $a_{\text{min}}$  and  $a_{\text{max}}$  being the minimum and maximum sizes of grains. We employed the standard value  $p = -3.5$ . Extinction and scattering opacities, scattering phase functions, and Mueller matrices are calculated using the Mie theory. We employed the astronomical silicates opacities of Draine & Lee (1984), the neutral PAH opacities computed by B. T. Draine (compiled from Laor & Draine 1993; Draine & Lee 1984; Li & Draine 2001), and the amorphous carbonaceous dust optical constants derived by Li & Greenberg (1997).

In summary, the free parameters of a model are the number of zones used to describe a disk, and for each zone  $R_{\text{in}}$ ,  $R_{\text{out}}$ ,  $p$ ,  $\beta$ ,  $q$ ,  $h/r$ , *edge*,  $M_{\text{dust}}$ , gas-to-dust ratio, and dust composition, and for each dust species  $a_{\text{min}}$ , and  $a_{\text{max}}$ .

Sub-mm continuum images were convolved with a 0.24'' × 0.5'' beam for comparison with SMA observations.

### 3.5. ProDiMo parameters

We used the cosmic ray ionization rate of H<sub>2</sub> of 5×10<sup>-17</sup> s<sup>-1</sup>. The incident vertical UV are set to the interstellar medium value. Non-thermal broadening is set to 0.15 km s<sup>-1</sup>. We use the UMIST chemical network (9 elements, 71 species connected through 950 reactions neutral-neutral, ion-molecule, photo-reactions, cosmic ray reactions and absorption & desorption of CO, CO<sub>2</sub>, H<sub>2</sub>O, NH<sub>3</sub>, CH<sub>4</sub>, see Woitke et al. 2009). UV fluorescence is included for [O I] and [C II] but not for CO. UV CO fluorescence has been included test wise later in the paper. A list of the species used is provided in Woitke et al. (2009).

### 3.6. CO 4.7 $\mu\text{m}$ data and slit effects

For our analysis, we downloaded the one-dimensional CO 4.7  $\mu\text{m}$  reduced spectrum used in Pontoppidan et al. (2008)<sup>4</sup>. We flux-calibrated the spectrum using the Spitzer flux at 4.7  $\mu\text{m}$  (see Appendix for the photometry) and measured the CO line fluxes by fitting a gaussian to their line profile. The CO P(1) to P(11) line profiles are available within the CRIRES spectrum. After subtraction of the continuum and normalization by the peak flux the lines have within the errors the same line profile (see Fig. A.3 in the Appendix) We selected the CO P(10) line for detailed modeling because the line profile is complete, is weakly affected by nearby strong telluric absorption lines, and has good S/N. The line CO P(10) line flux is 1.5×10<sup>-17</sup> W m<sup>-2</sup> with an error of the order of 20% due to slit losses and systematics.

To compare the ProDiMo predictions with the observed CRIRES CO 4.7  $\mu\text{m}$  spectra the effects of the slit width and orientation, the observing conditions, and spectral resolution needed to be taken into account.

ProDiMo generates channel maps data cubes, i.e., for each velocity bin, a 2D image of CO emission is generated (see details in Bertelsen et al. in prep.). The pixel size of the CRIRES detector in the spatial direction is 0.086'', at a distance of 140 tpc that corresponds to a pixel size of ~12 AU. We generated the ProDiMo data cubes with a pixel size of 2 AU.

The ProDiMo data cubes were first convolved in the spatial direction with a gaussian PSF of  $FWHM=180$  mas. Then they were convolved with a gaussian of  $FWHM=3.3$  km/s in the wavelength direction to simulate  $R=90\,000$  of the observations. A mask of 0.2'' (28 AU) with the correct PA was applied in each channel to mimic the slit. The fluxes were added in the direction perpendicular to the slit to generate a 2D spectrum.

In the 2D spectrum the centroid of the photo center at line velocity ( $v$ ) was calculated using (Pontoppidan et al. 2008)

$$X(v) = K \frac{\sum_i (x_i(v) - x_0) F_i(v)}{\sum_i F_i(v)} \quad (\text{pixels}) \quad (1)$$

where  $x_i - x_0$  is the center of pixel  $i$  relative the continuum centroid position, and  $F_i(v)$  is the flux on the pixel  $i$ .  $K$  is a correction factor to take into account that not all of the source flux is enclosed in the aperture (Pontoppidan et al. 2008). We used the value of  $K = 1.3$  used by Pontoppidan et al. (2008) in their analysis of the spectroastrometry signal of HD 135344B to be able to compare our models to their measurements. A 1D spectrum is further obtained by summing the pixels on the spatial direction. To compare the observed and synthetic line profiles, the spectra were normalized by dividing them by the median of the continuum, then after continuum subtraction, the profile was re-normalized by diving it by its maximum flux. In this way the continuum is always at 0 and the line peak is always at 1. The integrated line fluxes of the model (taking into account the slit effects) and the line profiles were compared independently to the observations.

## 4. Modeling Results

Before presenting the family of Models 5, the model that best describes the observations, in order to illustrate the reasoning

<sup>4</sup> Available in web-page of the CRIRES large program “*The planet-forming zones of disks around solar-mass stars: a CRIRES evolutionary survey*” (ESO-program 179.C-0151, PI: van Dishoeck & Pontoppidan) [http://www.stsci.edu/~pontoppi/Pontoppidan\\_web\\_home/CRIRES\\_Disks.html](http://www.stsci.edu/~pontoppi/Pontoppidan_web_home/CRIRES_Disks.html)

that lead us to this model, we describe very briefly the sequence of families of models we tested. A family of models is defined primarily by its dust properties (i.e., composition and location). We have extensively explored the parameter space in each family of models. However, we will limit the discussion to the parameter space on the family of Models 5. In Table 4 we present the details of a representative example of each family of Models. The different families of models show us the close relation that exists between the properties assumed for the dust (size distribution, composition, and mass) at the beginning of the modeling procedure and the gas lines obtained.

#### 4.1. Family of Models 1: A disk composed of astronomical silicate grains only

As starting point we assumed, the simplest model, an inner and outer disk composed of 100% astronomical silicates and a gas-to-dust ratio of 100 in the whole disk. The solutions all converged to the same disk structure, namely a narrow ring of dust at 0.16 to 0.21 AU with a dust mass of a few  $10^{-10} M_{\odot}$  with grains of size larger than  $10 \mu\text{m}$  (to reproduce the lack of  $10 \mu\text{m}$  silicate feature), followed by a large gap of 45 AU and an outer disk from 45 to 200 AU with dust mass of  $10^{-4} M_{\odot}$ . By changing the disk's geometrical parameters, we found a disk able to reproduce most of the observed gas line fluxes (see Model 1a in Tables 4 and 5). However, because in this model the warm gas is located in the narrow inner-most region, the CO ro-vibrational emission produced has a broad double peaked profile with FWHM  $\sim 50$  km/s that is inconsistent with the observed FWHM  $\sim 15$  km/s (see Model 1a in Fig. 3).

With the aim of producing CO ro-vibrational emission extending tens of AU and a narrower line profile, in Model 1b, we introduced gas (and dust) between 0.21 and 45 AU. We found that although up to  $10^{-8} M_{\odot}$  of dust and  $10^{-6} M_{\odot}$  of gas can be added and still fit the SED, the CO ro-vibrational line always displayed a broad double peaked profile with FWHM  $\sim 50$  km/s. We tested several flat and flared disks filling the cavity (see Model 1b in Fig. 3), but in all the cases the same result was found. *The optically thick inner-most disk of silicates required to fit the near-IR SED shields the material inside the cavity and does not permit to the gas at several AU to be sufficiently warm to contribute significantly to the CO ro-vibrational lines.* A change on the dust optical properties of the inner disk is required to allow ro-vibrational CO emission at tens of AU.

##### 4.1.1. PAH content

PAHs are an important ingredient to calculate the gas heating. To constrain the PAHs, we employed the *Spitzer-IRS* spectrum<sup>5</sup>. PAHs are implemented as a second dust component into MCFOST. Their properties (abundance and size) are passed to ProDiMo in order to compute the gas heating due to the photoelectric effect.

<sup>5</sup> For our analysis, we downloaded the *Spitzer/IRS* observations (AOR 3580672, PI: Houck) from the *Spitzer* archive and re-reduced the data. The Short-Low data were reduced using the FEPS pipeline (S18.18.0, see Bouwman et al. 2008). The Short-High and Long-High data were reduced with the c2d pipeline (S18.18.0, Lahuis et al. 2006). For the high resolution modules we used the PSF extraction method, which include correction for pointing uncertainties. The mid-IR spectrum of HD 135344B is characterized by the absence of the silicate feature at  $10 \mu\text{m}$ , and the presence of weak PAH emission at  $11.2 \mu\text{m}$ , and lack of other PAH emission features (Geers et al. 2006; Maaskant et al. 2013).

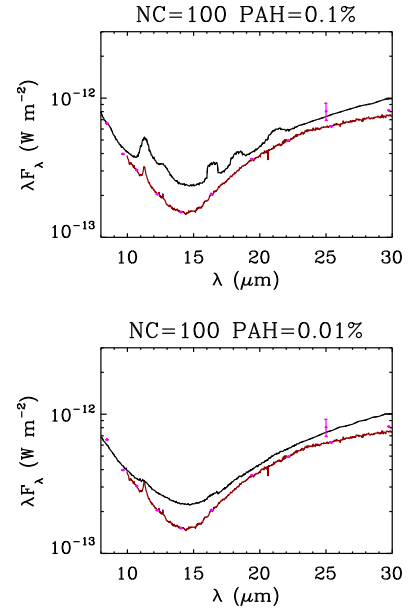


**Fig. 2.** Expected PAH spectrum (black) and *Spitzer* IRS spectrum (in red) for different dust mass fractions of neutral PAHs in the outer disk. In the rest of the paper, we used a 0.01% PAH fraction. NC = number of carbon atoms. Magenta points are photometry points (see Appendix).

Initially, we found that the observed  $11.2 \mu\text{m}$  PAH feature could be reproduced with neutral PAHs with 21 carbon atoms (NC=21) and 0.01% of the dust in the outer disk in the form of PAHs. However, such PAHs generated too much gas heating that translated in [O I]  $63 \mu\text{m}$  line fluxes 3 to 10 times stronger than the observations for almost all the models reproducing the SED. To have an [O I]  $63 \mu\text{m}$  emission compatible within a factor 3 of the observations, we increased the PAH size to NC=100 and used a 0.01% fraction in mass of the dust in form of PAHs ( $f_{\text{PAH}} = 6.0 \times 10^{-3}$  for a gas to dust ratio 100, see Fig.2).

#### 4.2. Family of Models 2: An inner disk composed of a uniform mixture of amorphous carbon and astronomical silicates

In order to modify the continuum optical depth of the inner disk and to make it possible for the gas at larger radii ( $R \gg 1 \text{ AU}$ ) to contribute to the CO  $4.7 \mu\text{m}$  emission, we introduced amorphous carbonaceous grains in the dust mixture in the family of Models 2. Amorphous carbonaceous grains are commonly employed to fit of SEDs of T Tauri and Herbig Ae/Be stars. We assumed first a carbonaceous/silicate grains ratio constant with radius. The fraction of carbon grains in the dust mixture sets the extension of the inner disk that fit the near-IR SED. The larger the fraction of carbon grains, the larger the inner disk that reproduces the near-IR continuum. With a 25% fraction of carbonaceous grains, an inner disk extending from 0.18 to 20 AU fits the near-IR SED (see Model 2a in Table 4). With a 5% carbon fraction an inner disk extending from 0.18 to 3 AU is required (Model 2b).

The introduction of amorphous carbon grains reduced by a factor of a few the total dust mass required to fit the near-IR SED, allowed for a dust size distribution with smaller grains in the inner disk (and fit the lack of  $10 \mu\text{m}$  silicate feature), and drastically changed the inner disk's optical continuum depth. These changes resulted in an optically thin inner disk at  $4.7 \mu\text{m}$ , thus a CO ro-vibrational emission entirely dominated by emis-

sion from the inner rim of the outer disk, and very narrow single peaked CO ro-vibrational line profile of width of a few km/s, inconsistent with the observations (see Fig. 3).

#### 4.3. Family of Models 3: An inner disk with a radial dependent mixture of carbon and silicates

The results of the families of Models 1 and 2 suggested that the solution was an intermediate inner disk structure between a narrow disk of 100% silicates and an extended inner disk with a large amount of carbonaceous grains. In the family of Models 3, we allowed for a radial dependent carbonaceous/silicates grains ratio.

We found that an inner disk of tens of AU composed of silicates, but enriched with a small amount ( $10^{-12} M_{\odot}$ ) of amorphous carbon grains at small radii ( $0.2 < R < 0.26$  AU) is able to reproduce the near-IR SED, while at the same time it make it possible for the CO located at several AU to contribute significantly to the CO ro-vibrational line flux, thus reproducing the observed CO P(10) line profile (see Fig. 3).

Assuming a gas-to-dust ratio of 100 for the whole disk and a carbon-enriched inner-disk, we tested a large number of models ( $\sim 50\,000$  MCFOST,  $\sim 1\,000$  ProDiMo) varying the geometry (i.e.  $h/r$ , flaring, surface density exponent) and dust mass for the inner and outer disks. We found that the CO-rovibrational line profile is reproduced by an inner disk extending tens of AU in which the *surface density is flat or increases as a function of the radius* (i.e. a positive power law surface density). Solutions with outer disks flared and anti-flared were found.

Several Models 3 reproduced the CO P(10) flux and line profile, the  $H_2$  infrared lines upper-limits, and the CO sub-mm and mm line fluxes (see one example in Tables 4 & 5). However, in all Models 3 calculated (covering a large range of geometries), the emission of [OI] 63 and 145  $\mu$ m, and the [C II] line at 157  $\mu$ m were over-predicted by factors larger than five. We tested several options available within ProDiMo (see Fig. 4) such as global gas-to-dust ratios lower than 100,  $H_2O$  ro-vibrational cooling (pure  $H_2O$  rotational cooling is calculated by default), lower metallicity, no PAHs, extremely low O/C abundances, but in most of the cases the [OI] 63 and 145  $\mu$ m lines were still too strong. We found that the only effective ways to significantly decrease the [OI] 63 and 145  $\mu$ m line fluxes were to assume  $T_{\text{gas}} = T_{\text{dust}}$ , or to *significantly* decrease the gas-to-dust ratio. The first is an extreme case of gas cooling that is unrealistic, as we now that  $T_{\text{gas}} > T_{\text{dust}}$  in the disk surface layer (e.g. Kamp & Dullemond 2004). The second, had the limitation that when the *global* gas-to-dust ratio was sufficiently low to describe the [OI] 63  $\mu$ m line, the CO ro-vibrational line was two orders of magnitude weaker. This last result indicated that the gas-to-dust ratio should be different for the inner and outer disk.

Another limitation of the family of Models 3 was the fit to the PIONIER near-IR visibilities. In a forthcoming paper (Benisty et al. in prep) ESO-VLTI PIONIER near-IR observations of HD 135344B and other transition disks will be presented in detail. In Fig. 5, we present the observed VLTI/PIONIER squared visibilities at 1.6  $\mu$ m and the predicted visibilities of Model 3. We see clearly that an inner disk starting at  $R_{\text{in}} = 0.2$  AU, is not compatible with the interferometry data. Near-emission in Model 3 is produced too far out.

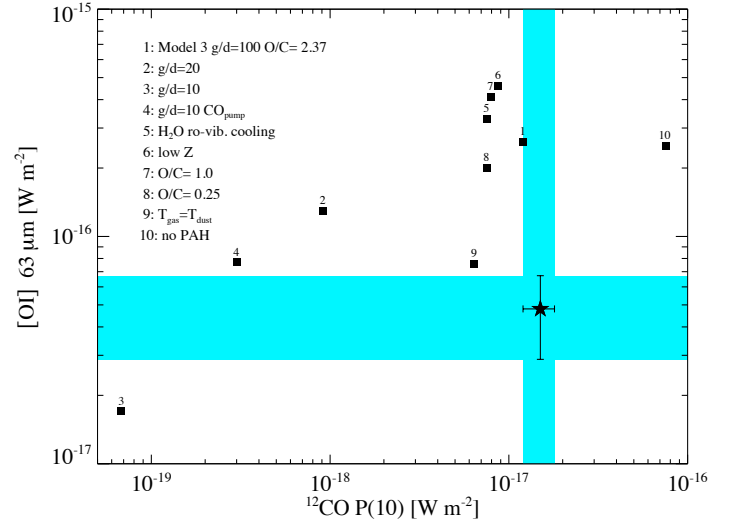


**Fig. 4.** Effect of changing different ProDiMo assumptions in the [OI] 63  $\mu$ m and CO P(10) line fluxes in one representative example of the family of Models 3. The star indicates the observed line fluxes. The cyan intervals represent the 20% error on the CO P(10) line flux and 40% error in the [OI] 63  $\mu$ m line flux. In the legend the symbols mean: g/d: gas-to-dust ratio;  $CO_{\text{pump}}$ : CO ro-vibrational emission calculated including UV fluorescent excitation;  $H_2O_{\text{cooling}}$ : gas temperature calculated including ro-vibrational water cooling (pure rotational  $H_2O$  cooling is always taken into account); low Z: low disk metallicity; O/C : oxygen over carbon abundance ratio;  $T_{\text{gas}} = T_{\text{dust}}$ : maximum possible cooling; no PAH: gas heating calculated without the effect of PAHs.

#### 4.4. Family of Models 4: Carbon grains inside the silicate sublimation radius, different gas-to-dust ratios for the inner and outer disk, and dust settling in the outer disk.

##### 4.4.1. The location of the carbonaceous dust

In the family of Models 3, the carbonaceous grains were located at  $R > 0.2$  AU to be consistent with the assumption that the temperature in the inner rim should not be higher than the silicate grains sublimation temperature ( $T \sim 1\,500$  K, for  $n_H \gtrsim 10^{16} \text{ cm}^{-3}$ , e.g. Helling et al. 2001). However, carbonaceous grains can survive temperatures higher than 1 500 K and up to 2 000 K (see for example Kobayashi et al. 2011). Therefore, one interesting possibility to physically justify the inner-disk carbon enrichment is that the carbonaceous grains are located inside 0.2 AU, the region where silicate grains sublimate. The survival of carbonaceous grains in this region will be discussed in Section 6.2.

Therefore for the family of Models 4, we located the carbonaceous grain component at  $0.08 < R < 0.2$  AU,  $R_{\text{in}}$  equal to the corotation radius, and  $R_{\text{out}}$  equal to the silicates sublimation radius. The astronomical silicate grains component of the inner disk was set to start at 0.2 AU. With this inner disk configuration we obtained an excellent match to SED and the PIONIER visibilities and closure phases (see Fig. 5). In our models the temperature at the innermost radius is  $\sim 2\,000$  K.

##### 4.4.2. Decreasing the [OI] 63 $\mu$ m emission

One limitation of the family of Models 3 was that it produced too strong [OI] 63  $\mu$ m line fluxes. The [OI] 63  $\mu$ m line is pro-

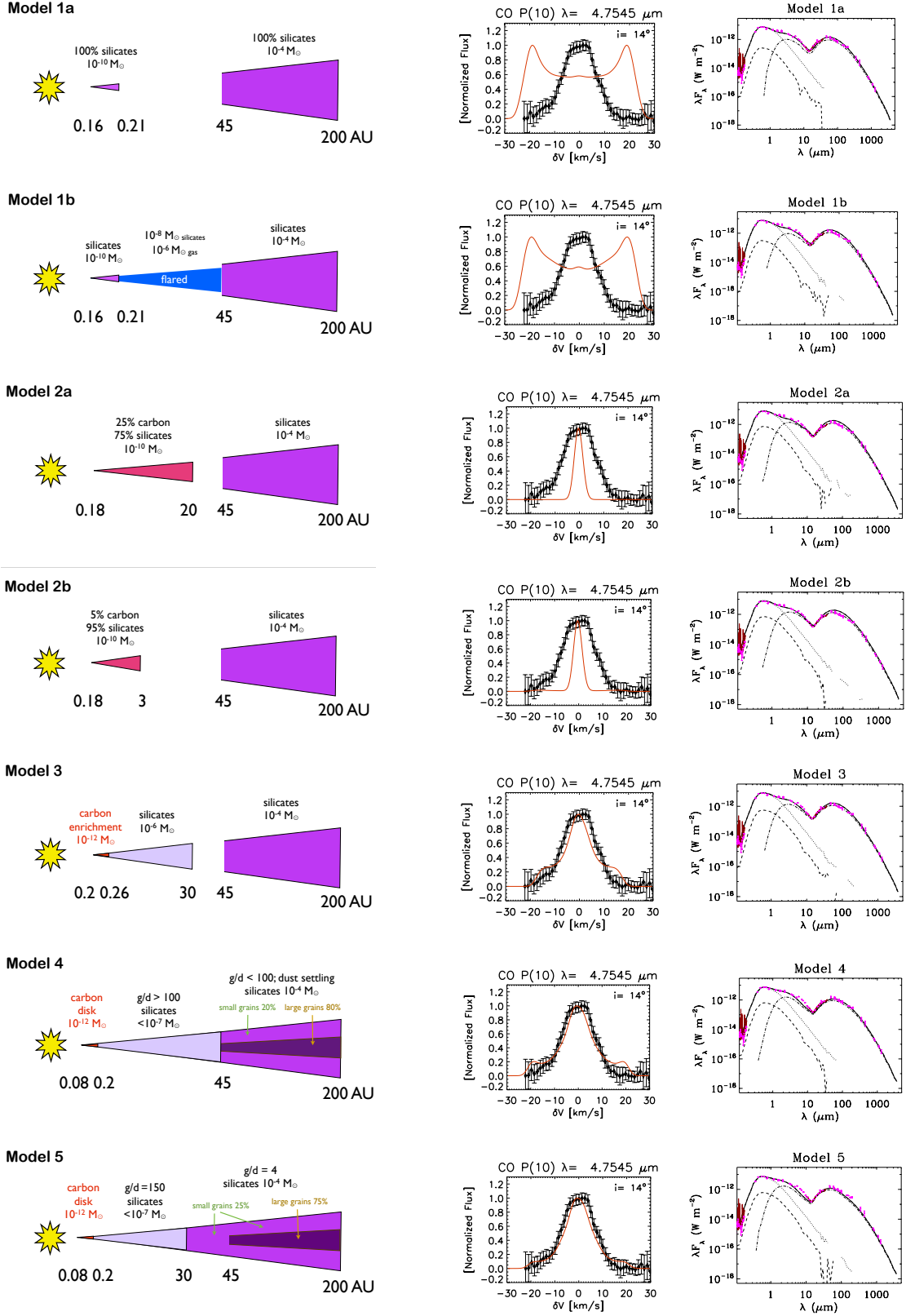


**Fig. 3.** Cartoon displaying the disk structure of the family of models tested, together with the CO P(10) line profile and SED predicted. The CO P(10) line profile includes the effects of the slit and it is displayed for PA of the slit of  $180^{\circ}$ . A representative example of each family of models is shown. In the SED plots the dotted line is the star emission, the dash-dotted line is the dust thermal emission, and the dashed line is the dust scattered light emission. Details of the models are presented in Table 4 and the predicted lines fluxes are given in Table 5.

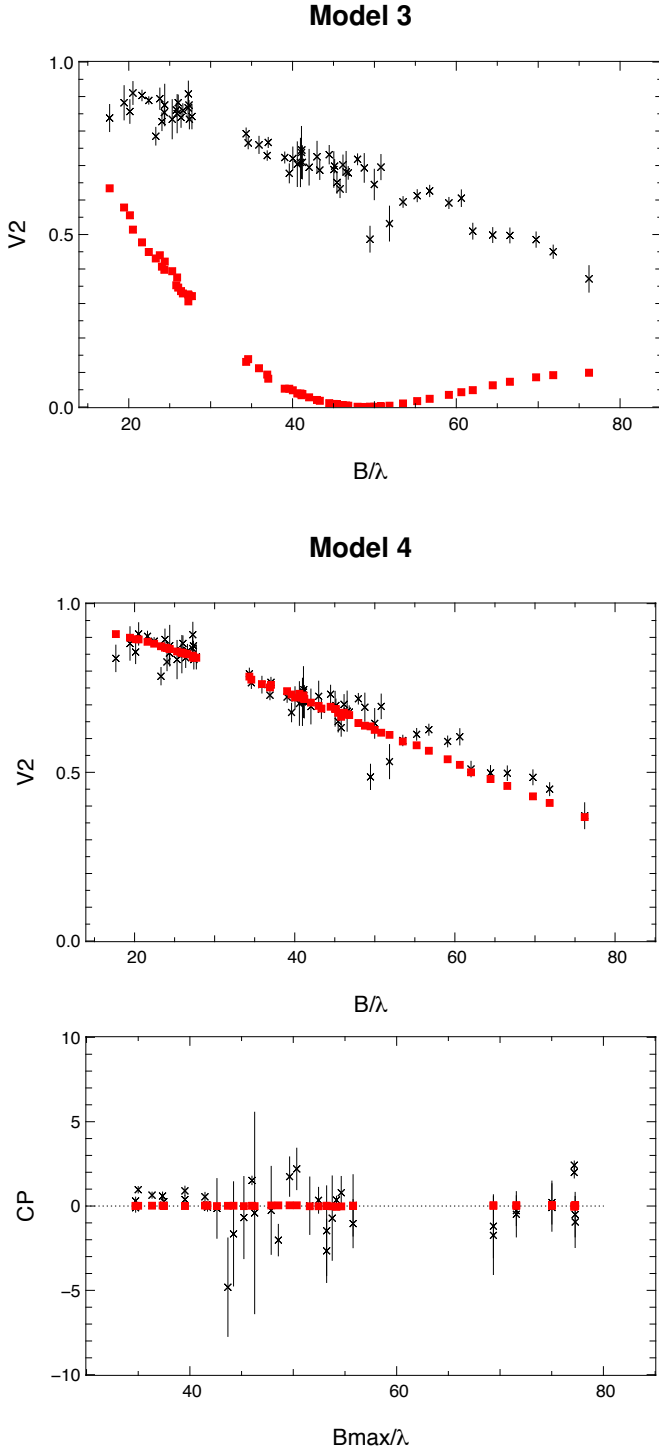


**Fig. 5.** Upper panel: Squared visibilities (in red) of Model 3 over-plotted onto the observed  $1.6 \mu\text{m}$  VLT/PIONIER visibilities (in black). An inner disk starting at 0.2 AU is not consistent with observations. VLT/PIONIER data clearly shows that there is material at smaller radii (i.e. inside the silicate sublimation radius). Central panel: Squared visibilities (in red) predicted by Model 4 ( $R_{\text{in}} = 0.08 \text{ AU}$ ). Lower panel: Closure Phases (CP) predicted by Model 4 (red) and measured by VLT/PIONIER (black).

duced partly by gas inside the cavity between 10 and 45 AU, but principally by gas in the outer disk between 45 and 60 AU. As

the surface density and gas mass in the inner disk are set by CO ro-vibrational line, to lower the [O I] line fluxes three modifications to the family of Models 3 were introduced in the family of Models 4:

1. the gas-to-dust ratio in the outer disk was allowed to be lower than 100,
2. the surface density of the outer disk needed too be shallower (we obtained good solutions with  $q = -1.0$ , similar to the surface density power law exponent found by Andrews et al. (2011) from SMA sub-mm continuum observations)
3. the scale height of the outer disk needed to be lower than 10%.

These changes on the outer disk geometry entrained a bad fit of SED at  $\lambda > 15 \mu\text{m}$ . To resolve this, a fourth modification was introduced in the outer disk by splitting it in two superposed disks. A first disk with lower H/R (5%), 80% of the gas and dust mass, and with a dust population of large grains ( $0.01 < a < 1000 \mu\text{m}$ ); and a second disk with higher H/R (0.8-0.13), the 20% remaining gas and dust mass, and with a dust population of smaller grains ( $0.01 < a < 10 \mu\text{m}$ ). This modification aims to keep most of the gas mass of the outer disk at low H/R (to fit the [O I]  $63 \mu\text{m}$  line) while allowing some small dust particles to be present in an extended outer disk atmosphere at higher H/R to fit the SED at  $\lambda > 15 \mu\text{m}$ . This two-layered outer disk echoes the expected effect by dust coagulation and sedimentation (i.e. large grains closer to the mid-plane).

Finally, concerning the inner disk, to address the fact that scattered light imaging (Muto et al. 2012; Garufi et al. 2013) revealed material inside the cavity down to 28 AU, we set, as a first approximation, the inner disk to have an outer radius of 45 AU, such that the whole cavity is replenished with gas, and we allowed the gas-to-dust ratio to be larger than 100 in the inner disk to be able to have sufficiently high CO  $4.7 \mu\text{m}$  emission.

With this ensemble of modifications, we found a family of disk models able to describe simultaneously the SED, the CO P(10) line profile, the line fluxes of [O I]  $63 \mu\text{m}$  (within a factor 2), CO P(10) (within a factor 4),  $^{12}\text{CO}$  3-2,  $^{12}\text{CO}$  2-1, and the upper limits of [O I] at  $145 \mu\text{m}$ , [C II] at  $157 \mu\text{m}$ , and the  $\text{H}_2$  lines in the near and mid-IR. The properties of a representative model of the family of Models 4 is described in Table 4, the line fluxes predicted are presented in Table 5.

The family of Models 4 confirmed the result that to describe the CO P(10) line profile the gas in the inner disk should be distributed with a *surface density increasing as a function of the radius*, and indicated that to describe the [O I]  $63 \mu\text{m}$  line flux observed by Herschel, *the gas-to-dust ratio in the outer disk should be much lower than 100*. The best match to the Herschel lines [O I]  $63 \mu\text{m}$  was obtained by a gas-to-ratio below 10, nevertheless, gas-to-dust ratios up to 40 provided [O I]  $63 \mu\text{m}$  fluxes within a factor 2 of the observations.

#### 4.5. Family of Models 5: Introducing recent constraints from polarized and mid-IR imaging.

In a recent work Garufi et al. (2013) showed that polarized scattered light in HD 135344B drops significantly at a radius of 28 AU. A lack of polarized emission can be the signature of either a lack of material or a change on the illumination of material inside the cavity. Similarly Maaskant et al. (2013) proposed a cavity of size 30 AU based on modeling of the SED and mid-IR imaging. The detection of scattered light down to 28 AU, inside the sub-mm dust cavity of 45 AU, indicates a different spatial location for the small and large dust grains in the outer disk.



To account for the recent results from Garufi et al. (2013), we slightly modified the disk structure of the family of Models 4. First we shortened the outer radius of the inner disk to 30 AU and decreased its dust mass to keep it consistent with the SMA 870  $\mu\text{m}$  upper limit. Second, we extended the small particle component of the outer disk down to 30 AU. The large grain component of the outer disk was kept at 45 AU to account for the sub-mm 870  $\mu\text{m}$  imaging constraints.

With these modifications, we obtained a disk structure compatible with the Garufi disk structure, while keeping the fit to the SED and the gas lines. Our model has gas and (some) dust inside 30 AU to account for the extended CO ro-vibrational line observed. However, note that the amount of dust at  $R < 30$  AU ( $< 10^{-7} M_{\odot}$ ) is much lower than the amount of dust the outer disk ( $2 \times 10^{-4} M_{\odot}$ ). The properties of a representative model of the family of Models 5 is described in Table 4, the line fluxes predicted are presented in Table 5. In Fig. 6, we present the synthetic SED, the predicted CO P(10) line profile and spectroastrometry signal, and the plots describing the optical depth of the line and of the continuum, the cumulated line flux intensity, and the number density of the species as function of the radius for the CO P(10), [O I] 63  $\mu\text{m}$ , and CO 3-2 lines at 870  $\mu\text{m}$  lines. Fig. 6 presents also a plot of a surface density of the gas and the dust as a function of the radius. In Fig. A.4 in the Appendix, we present the plots of the number density of H as a function of the radius, the dust and gas temperature in the disk, and similar plots as in Fig. 6 but for the [O I] 145  $\mu\text{m}$ , [C II] 157  $\mu\text{m}$ , and H<sub>2</sub> 0-0 S(1) 17  $\mu\text{m}$  lines.

## 5. Disk structure constraints derived from Model 5.

The interest of performing multi-instrument modeling is to use the constraints obtained from different gas and dust tracers to break the model degeneracies and narrow down the parameter space of possible solutions. Ideally, a Bayesian analysis of a large number of models covering a significant fraction of the parameter space should be performed. However, due to the prohibiting amount of computing time that this kind of analysis would require when the heating and cooling balance and the chemistry calculation is included, we limit our discussion to the parameter space surrounding Model 5, the best solution found. Our solution is a model that reproduces most of the constraints imposed by observations, however, there is the possibility that this the solution is *not* unique.

### 5.1. Compromises done during the modeling procedure

Ideally, a model should be able to reproduce all the observations available. However, to be able to reproduce simultaneously most of the observations, we needed to relax the perfect fit for a few of them. ProDiMo has an important number of physical processes included, however, not all the physics are included in the code. Furthermore our models are axisymmetric. HD 135344B is known to display a spiral structure (Muto et al. 2012; Garufi et al. 2013). Not including these spiral structures may have an impact, or not, on the integrated line fluxes that we are fitting. But, we are modeling integrated quantities, spiral arms produce local changes, thus, it is not clear whether their impact would be dramatic.

The first compromise is the fit to near-IR SED at 8-10  $\mu\text{m}$ . Our model is fainter than the observations at those wavelengths. Provided a carbon inner-most disk that reproduces the near-IR interferometry data and the SED near-IR excess, for a given silicates dust size distribution, one can construct a disk between

0.2 to 30 AU with sufficient dust mass, such that 8 to 20  $\mu\text{m}$  excess is well reproduced (see for example Model 3). However, the upper limit of the continuum emission at 870  $\mu\text{m}$  inside 30 AU sets a stringent limit to the amount of dust mass that can be put in the inner disk. Higher masses can be achieved using smaller grain size distributions, however, when the dust size distribution is dominated by dust with  $a_{\text{min}} < 10 \mu\text{m}$  then the silicate feature appears. A solution to better fit the near-IR SED might be to introduce an additional zone at higher H/R in inner disk with small grains ( $a_{\text{min}} < 10 \mu\text{m}$ ) with 1 to 10% of the inner disk mass.

The second compromise is the absolute flux of the CO ro-vibrational lines. A cavity without discontinuity in the gas implies that around half of the [O I] 63  $\mu\text{m}$  and 145  $\mu\text{m}$  lines will be emitted *inside* the cavity (see Fig. 6). Therefore, when the gas mass or temperature is increased to better fit the CO P(10) flux, the flux of the [O I] lines will also increase. As the [O I] 63 and 145  $\mu\text{m}$  excitation is better understood and tested than CO ro-vibrational excitation (the collision rates are known only within a factor ten (Thi et al. 2013)), and because the [O I] 63  $\mu\text{m}$  line can be used to constraint the gas mass, we gave priority to fit the [O I] 63  $\mu\text{m}$  and 145  $\mu\text{m}$  line fluxes and upper limits simultaneously with the CO P(10) line-profile, than to reproduce the CO P(10) absolute line flux. Our models under-predict the CO P(10) line flux, hence the spectroastrometry signature.

### 5.2. Inner disk surface density exponent

The CO P(10) line-profile strongly depends on the surface density power law exponent of the inner disk gas. In Fig. 7, we display the calculated CO P(10) line profile after taking into account the slits effects for disks with inner and outer disk H/R ranging from 0.07 to 0.15, and  $q$  ranging from -0.4 to +0.6. The CO P(10) line profile is best described by slightly positive power-law surface density exponents, in other words by a *surface density that increases as a function of the radius*. Power law exponents  $q$  smaller than 0.0 produce too broad line profiles,  $q$  larger than +0.4 produce too narrow line profiles. Keeping in mind the uncertainties and simplifications in the ProDiMo code, we can exclude gas surface density profiles with negative exponents for the inner disk. A steep surface density profile with a negative exponent will assign too much gas in the inner few AU of the disk. This would result in too much hot CO gas emitting close to the star and at high-velocities which is in contradiction with the line profile and spectroastrometric signal observed, that show that the CO ro-vibrational emission comes from radii greater than a few AU.

This result is relatively independent of the scale-height assumed for the inner disk. Here we have assumed that the CO 4.7  $\mu\text{m}$  line is entirely produced by disk emission. Although a contribution from a weak disk wind can not be ruled out (the object display asymmetric oxygen emission at 6300 Å, van der Plas et al. 2008) the symmetric spectroastrometry signature detected by Pontoppidan et al. (2008) at three slit positions favors a dominant contribution from disk emission.

Despite that all the cavity is filled with gas, the predicted spectroastrometry signature of our models is a factor 2 lower than the observations by Pontoppidan et al. (2008) and the line flux is weaker than the line flux observed. As we fit the line profile, the relative contributions to the flux by the different radii should be correct. The missing flux might be related to a CO heating-mechanism or CO physics not yet included in ProDiMo.



## Model 5

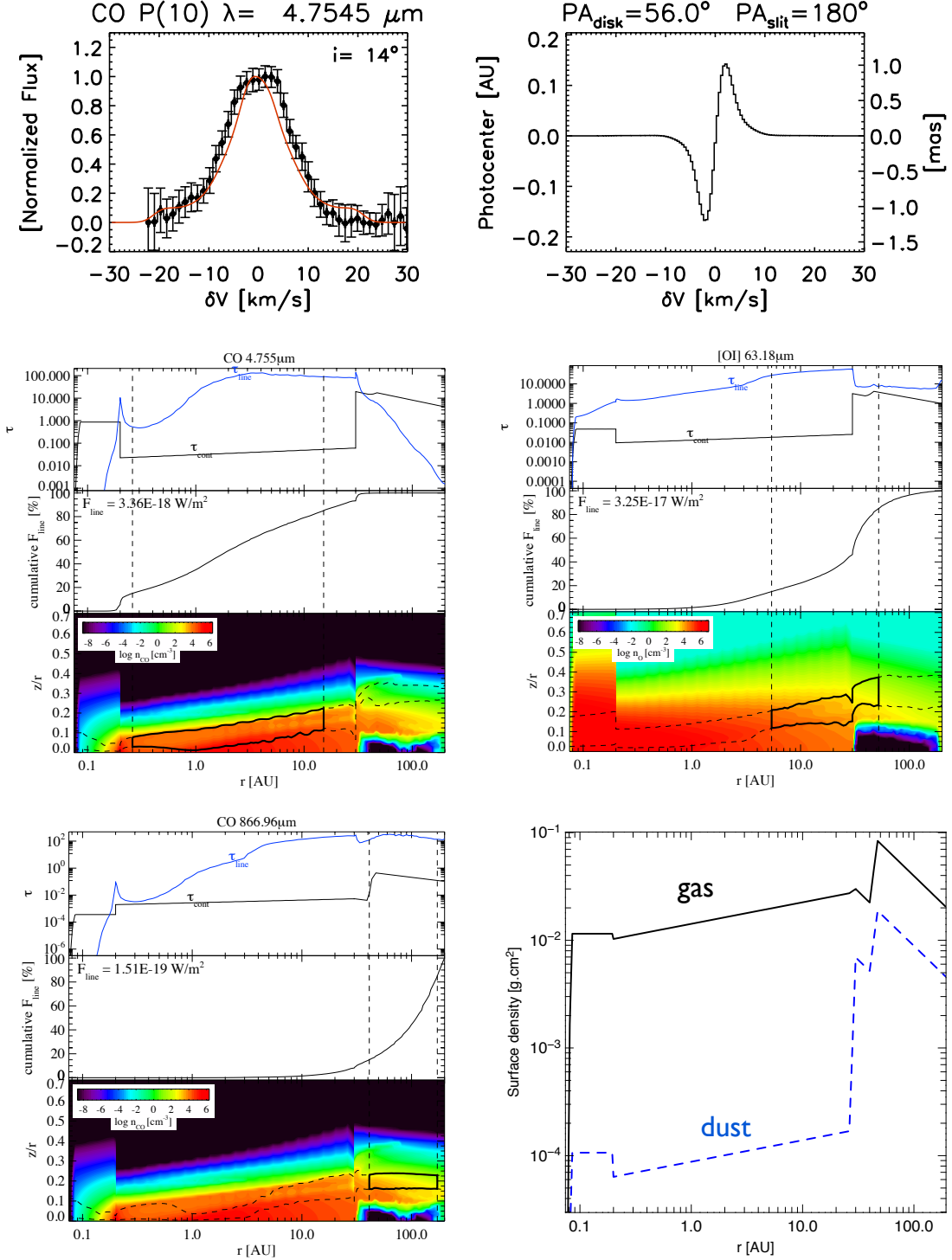


**Fig. 6.** *Upper panels:* CO P(10) profile (left) and expected spectroastrometry signature (right) for Model 5. *Central Panels* optical depth of the line and of the continuum, cumulative line flux, number density, and emitting region diagrams for the CO P(10) (left) and [OI] line at 63  $\mu\text{m}$  (right) lines. The box in thick black lines represents the region in the disk that emits 70% of the line radially and 70% of the line vertically, thus approximately  $\sim 50\%$  of the line flux. *Lower Panels:* (left) Similar plots for the  $^{12}\text{CO}$  3-2 line at 870  $\mu\text{m}$ , (right) surface density of the gas (black continuous line) and the dust (blue dashed line) as a function of the radius. The surface density distribution of the gas at  $R < 30$  AU increases with radius. Note the change on the gas-to-dust ratio between the inner and outer disk. The line fluxes quoted in the panels are the total integrated line fluxes. In the case of the CO P(10) line the flux is the total flux from the disk. For the integrated line flux taking into account the slit losses see Table 5. Extra information about the model is presented in Fig. A.4 in the Appendix.

**Table 4.** Summary of model parameters

	Zone	$\beta^\dagger$ [ $M_\odot$ ]	$M_{dust}$ [AU]	$R_{in}$ [AU]	$R_{out}$ [AU]	edge [AU]	$q^{\dagger\dagger}$	H/R	Dust type	$a_{min}$ [ $\mu m$ ]	$a_{max}$ [ $\mu m$ ]	$f_{PAH}$	g/d
Model 1a	<b>Only astronomical silicates. No gas in the gap</b>												
	1	1.10	7.0E-10	0.16	0.21	0.002	-1.5	0.016/ 0.10	Astro-Silicates	10.00	1000.00		100
	2	1.00	1.1E-04	45	200	1.0	-2.5	4.5/ 45	Astro-Silicates	0.05	1000.00	6.5E-3	100
Model 1b	<b>Only astro. silicates. Gas in the gap.</b>												
	1	1.10	7.0E-10	0.16	0.21	0.002	-1.5	0.016/ 0.10	Astro-Silicates	10.00	2000.00		100
	2	1.10	1.0E-08	0.21	40	0.0	-1.0	0.015/ 0.10	Astro-Silicates	10.00	2000.00		100
	3	1.00	1.1E-04	45	200	1.0	-2.5	4.5/ 45	Astro-Silicates	0.05	1000.00	6.5E-3	100
Model 2a	<b>25% carbon grains inner disk</b>												
	1	1.25	1.8E-10	0.18	20	0.001	-1.5	0.012/ 0.10	Amor. Carbon	0.01	10		100
	2	1.00	1.0E-04	45	200	1.0	-2.5	5.5/ 45	Astro-Silicates	0.05	1000	6.5E-3	100
Model 2b	<b>5% carbon grains inner disk</b>												
	1	1.00	3.0E-10	0.18	3	0.001	-2.0	0.010/ 0.10	Am. Carbon	0.01	10		100
	2	1.00	1.1E-04	45	200	1.0	-2.5	6.0/ 45	Astro-Silicates	0.05	1000	6.5E-3	100
Model 3	<b>carbon-enriched inner-most disk (<math>0.2 &lt; R &lt; 0.25</math> AU), g/d = 100 in the whole disk</b>												
	1	1.00	6.0E-12	0.21	30	0.002	-5.0	0.010/ 0.10	Am. Carbon	0.01	10		100
	2	1.00	1.0E-06	0.21	30	0.002	0.25	0.015/ 0.10	Astro-Silicates	100	2 000		100
	3	0.60	1.0E-04	45	200	1.0	-2.0	6.3/ 45	Astro-Silicates	0.05	1000	6.5E-3	100
Model 4	<b>inner disk: carbon grains <math>0.1 &lt; R &lt; 0.2</math>, silicates 0.2 to 45 AU, (g/d)<sub>inner</sub>=150 ; outer disk: dust settling, (g/d)<sub>outer</sub>=2; continuous gas surface density at 45 AU</b>												
	1	1.10	2.5E-12	0.085	0.20	0.002	0.0	0.012/ 0.10	Am. Carbon	0.01	10		150
	2	1.12	3.5E-07	0.20	44	0.0	0.30	1.2/10	Astro-Silicates	0.10	1 000		150
	3	1.0	0.4E-04	45	200	0.0	-1.0	1.2/10	Astro-Silicates	0.01	10	0.18	2
	4	1.0	1.6E-04	45	200	0.0	-1.0	0.5/10	Astro-Silicates	0.01	1 000	0.18	2
Model 5	<b>inner disk: carbon grains <math>0.1 &lt; R &lt; 0.2</math>; silicates 0.2 to 30 AU; outer disk: small dust dust down to 30 AU, large dust down to 45 AU</b>												
	1	1.10	2.5E-12	0.085	0.20	0.002	0.00	0.012/ 0.10	Am. Carbon	0.01	10		100
	2	1.12	1.0E-07	0.20	30.00	0.0	0.20	1.1/10	Astro-Silicates	0.10	1 000		150
	3	1.00	0.5E-04	30.00	200.00	0.0	-1.00	1.1/10	Astro-Silicates	0.01	10	0.09	4
	4	1.00	1.5E-04	45.00	200.00	1.0	-1.00	0.7/10	Astro-Silicates	0.01	1 000	0.09	4

Notes:  $^\dagger \beta$  is the flaring exponent;  $^{\dagger\dagger} q$  is the surface density exponent.

**Table 5.** Observed and modeled line fluxes.

	[O I] 63 $\mu m$	[O I] 145 $\mu m$	[C II] 157 $\mu m$	$^{12}CO$ J3-2 866 $\mu m$	$^{12}CO$ J2-1 1.3mm	$\nu=1-0$ P(10) <sup>a</sup> 4.7545 $\mu m$	H <sub>2</sub> 1-0S(1) 2.12 $\mu m$	H <sub>2</sub> 0-0S(1) 17.03 $\mu m$
<b>Observed</b>	3.6–4.8E-17	<4.6E-18	<6.4E-18	1.2E-19	8.0E-20	1.5E-17	<1.6E-17	< 1.0E-17
Model 1a	5.4E-17	4.4E-18	3.7E-18	2.3E-19	7.4E-20	1.6E-17 74%	8.2E-20	1.9E-19
Model 1b	7.2E-17	5.5E-18	4.7E-18	2.5E-19	7.8E-20	1.7E-17 74%	1.8E-19	4.4E-19
Model 2a	2.7E-16	1.8E-17	8.7E-18	2.6E-19	8.0E-20	1.5E-17 21%	5.4E-18	9.4E-18
Model 2b	3.4E-16	2.8E-17	1.2E-17	3.3E-19	1.0E-19	7.4E-17 26%	8.7E-18	1.2E-17
Model 3	2.6E-16	2.0E-17	1.2E-17	2.8E-19	8.5E-20	1.2E-17 66%	1.5E-18	4.6E-18
Model 4	4.0E-17	2.4E-18	2.2E-18	1.6E-19	5.0E-20	3.7E-18 72%	5.4E-19	2.6E-19
Model 5	3.2E-17	1.5E-18	1.7E-18	1.5E-19	4.7E-20	2.5E-18 72%	6.0E-19	1.8E-19

Notes: <sup>a</sup> The percentage after the CO P(10) line-flux, correspond to the fraction of line flux retrieved inside the slit.

### 5.3. Inner and outer disk scale height

We have set the scale height at the reference radius of 10 AU to be the same for the inner disk and the small dust grain component of the outer disk. In Figure 8b, we display the effect of changing the scale height, the power law exponent of the surface density of the inner disk, and the gas-to-dust ratio of the outer disk in the flux of the [O I] 63  $\mu m$  line.

The [O I] 63  $\mu m$  line flux changes little with a change on the surface density of the inner disk, and is slightly sensitive to changes on the scale height of the inner and outer disk. In general, larger H/R values produce larger [O I] 63  $\mu m$  fluxes. However, note that the mild sensitivity in the H/R of the outer disk is because most of the gas mass in the outer disk is in its

mid-plane layer that has lower H/R and large grains. Changes on the scale height of the small dust extended outer disk atmosphere change little the [O I] 63  $\mu m$  line flux because its mass is low with respect to that of the mid-plane.

*The scale height of the disk is principally constrained by the SED fit.* In Figure 8a, we show three insets displaying the SEDs for Models 5 with H/R 0.7, 0.11 and 0.15. The SED is compatible with Models 5 with an H/R between 0.9 and 0.13. Disks with H/R lower than 0.9 underestimate the flux at  $\lambda > 10 \mu m$  region, disks with H/R larger than 0.13 overestimate the flux in the 10 - 100  $\mu m$  region.

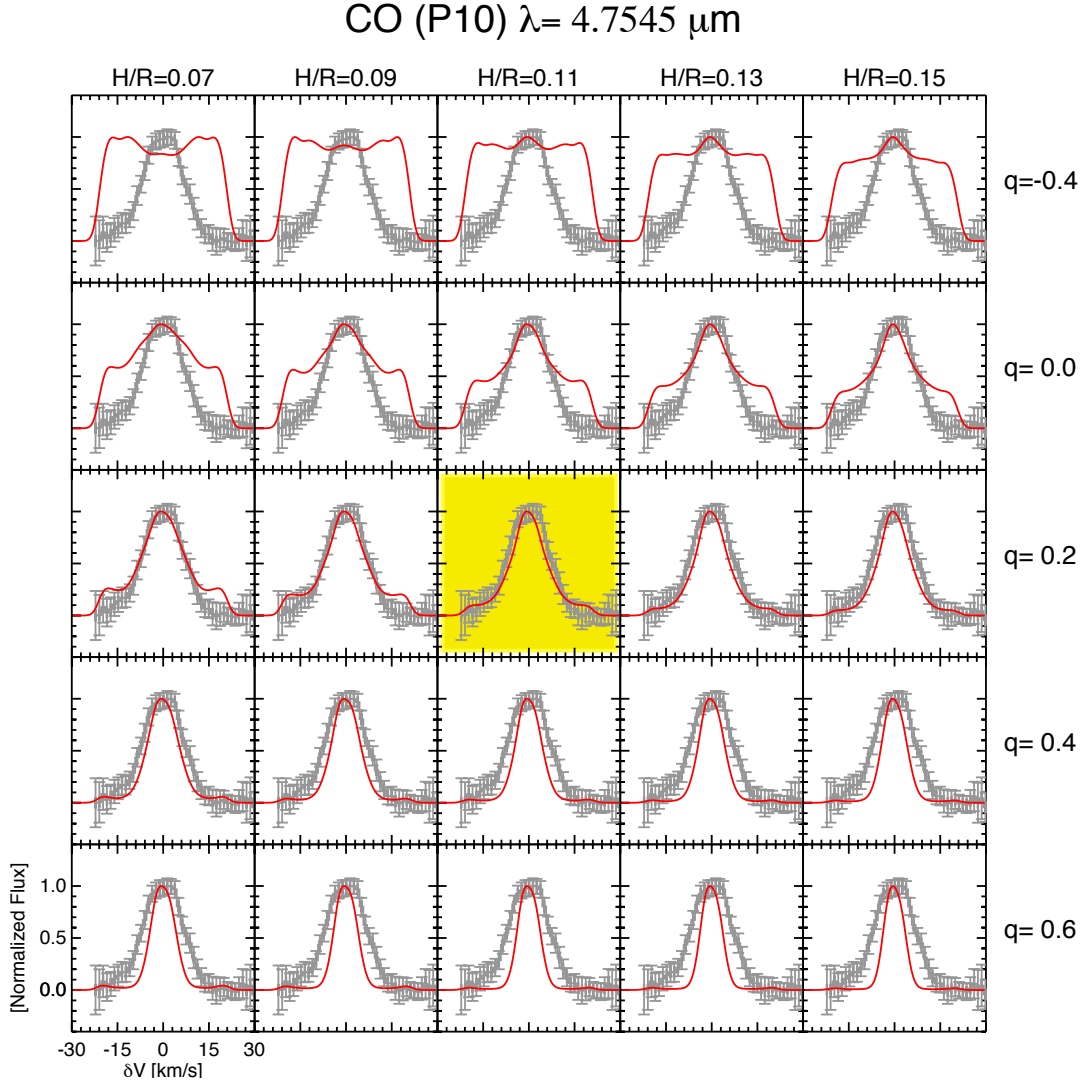


**Fig. 7.** CO P(10) line profiles for diverse values of  $H/R$  and the surface density exponent of the inner disk  $q$  in the family of Models 5. The reference radius of  $H/R$  is 10 AU.  $H/R$  is the same for the inner and the outer disk. All other parameters of Model 5 are kept constant. The best fit is highlighted.

#### 5.4. Outer disk's gas-to-dust ratio

The fit to the SED provides a relative robust estimate of the mass of mm-size grains in the outer disk. This value changed little on all the models tested and is of the order of  $2 \times 10^{-4} M_{\odot}$ . The gas mass, thus the gas-to-dust ratio, in the outer disk is constrained by the simultaneous fit to the [O I]  $63 \mu\text{m}$  line flux and the CO P(10) line profile.

Figure 8b displays the flux of the [O I]  $63 \mu\text{m}$  as a function of  $H/R$  for gas-to-dust ratios of the outer disk ranging from 1 to 100. We can see, that the flux of the [O I]  $63 \mu\text{m}$  line is very sensitive to the value of the gas-to-dust ratio in the outer disk. We find that the [O I]  $63 \mu\text{m}$  line flux is preferentially described by models with gas-to-dust ratios in the outer disk much lower than 100. Gas-to-dust ratios between 25 and 4 provide the best fit to line flux for the scale heights that are compatible with the SED.

In all the models the [O I]  $145 \mu\text{m}$  line flux is below the Herschel flux-upper limits. In all the models CO sub-mm lines are so optically thick ( $\tau > 100$  see Fig. 6) that decreasing the gas

mass does not affect the line fluxes, thus these can not be used to trace the gas mass.

The amount of gas in the inner rim of the outer disk influences the shape of the CO P(10) profile making it more centrally peaked when more gas is present in the outer disk (see Fig. 8c). The best fit to the CO P(10) line is given by gas-to-dust ratios in the outer disk below 10.

The exact value of the gas-to-dust ratio in the outer disk is model dependent. However, as most of the models describing simultaneously the [O I]  $63 \mu\text{m}$  line flux, the SED, and the CO P(10) line profile require gas-to-dust ratios for the outer disk smaller than 10, we believe that a gas-to-dust ratio much lower than 100 in the outer disk is a robust result.

Finally, the simultaneous modeling of the CO P(10) line profile and [O I]  $63 \mu\text{m}$  line flux favors models in which the the gas surface density contrast between the inner and the outer disk at the inner rim of the outer disk is smaller than a factor 20.

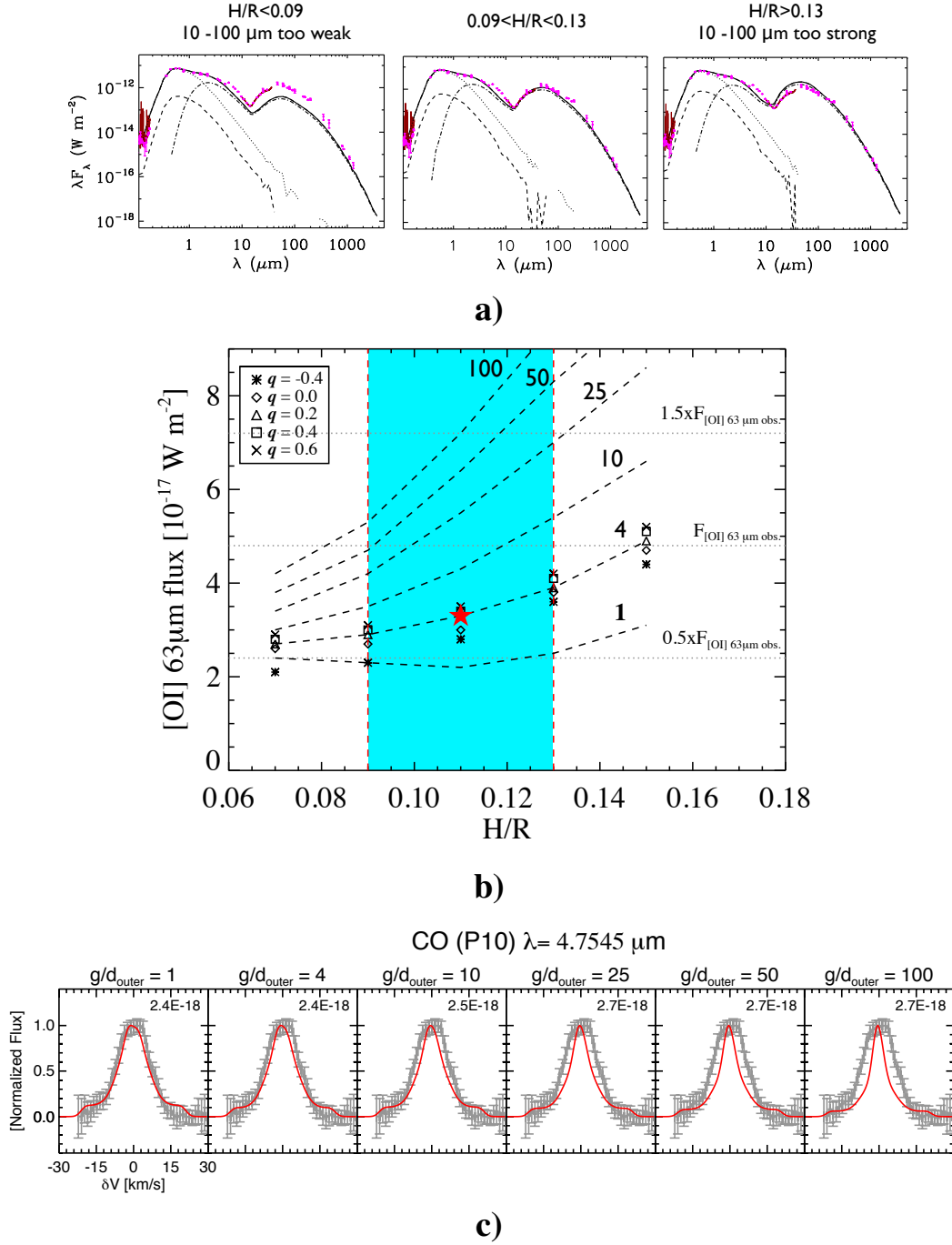


**Fig. 8.** *Top panels:* SED for disks with different values of H/R in the family of Models 5. The reference radius employed is 10 AU and H/R is set to be the same for the outer and the inner disk. In color cyan the allowed range of H/R consistent with the SED. *Central Panel:* Flux of the [O I] line at 63  $\mu\text{m}$  as a function of H/R for surface density exponents of the inner disk ranging from -0.4 to +0.6 (see legend) for a gas-to-dust ratio of the outer disk equal to 4. The dashed lines show the line flux for different gas-to-dust ratios of the outer disk for a constant inner disk surface density exponent  $q = 0.2$ . *Bottom Panels:* Expected CO P(10) profiles for different values of the gas-to-dust ratio in the outer disk for the family of Models 5 assuming  $H/R=0.11$  and  $q = 0.2$ . The number on the top right of each panel is the CO P(10) line flux in  $\text{W m}^{-2}$ . The star represents the values of Model 5 in Table 4 and Fig. 6. The best combined fit of the [O I] 63  $\mu\text{m}$  line flux and the CO P(10) line profile is given by gas-to-dust ratios below 10 in the outer disk.

### 5.5. Inner disk's gas mass, dust mass, and gas-to-dust ratio

For a given dust composition and size distribution, the SMA 870  $\mu\text{m}$  photometry upper limit of 10.5 mJy in a  $34 \times 70$  AU beam centered on the star (Andrews et al. 2011) sets the max-

imum amount of dust that can be located inside 30 AU almost independently of the surface density power law exponent and the scale height of the inner disk. With currently available data, the dust size distribution can not be constrained.

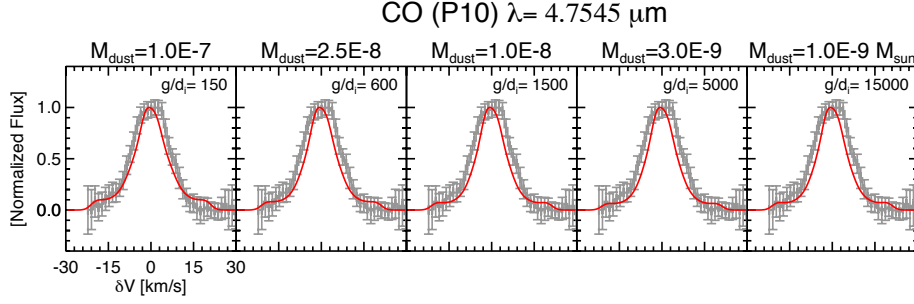


**Fig. 9.** CO P(10) line profiles as a function of the gas-to-dust ratio in the inner disk in Model 5. The gas mass ( $1.5 \times 10^{-5} M_{\odot}$ ) and gas surface density (see Fig. 6) at  $R < 30$  AU is kept constant. The carbon inner disk mass is kept constant. The outer disk is kept constant. We decreased the mass of silicates at  $0.2 < R < 30$  AU up to a factor 100 from left to right.

**Table 6.** Predicted continuum fluxes for Model 5 at  $R < 30$  AU for diverse values of the astronomical silicates dust mass at  $0.2 < R < 30$  AU for different grain sizes. The gas mass at  $R < 30$  AU is kept constant and equal to  $1.5 \times 10^{-5} M_{\odot}$ .

0.2 < R < 30 AU		0.1 < a < 1000		0.1 < a < 100		0.1 < a < 10	
Silicate Dust Mass	gas/dust <sub>inner</sub>	430 $\mu$ m	870 $\mu$ m	430 $\mu$ m	870 $\mu$ m	430 $\mu$ m	870 $\mu$ m
$M_{\odot}$		mJy	mJy	mJy	mJy	mJy	mJy
$1.0 \times 10^{-7}$	150	13.4	1.6	17.1	0.4	3.5	0.2
$5.0 \times 10^{-8}$	300	8.2	0.9	10.3	0.3	3.0	0.3
$2.5 \times 10^{-8}$	600	5.5	0.6	6.7	0.2	2.8	0.2
$1.0 \times 10^{-8}$	1500	3.8	0.3	4.3	0.2	2.7	0.2
$3.0 \times 10^{-9}$	5000	3.0	0.2	3.2	0.2	2.7	0.2
$1.5 \times 10^{-9}$	10000	2.8	0.2	3.0	0.2	2.7	0.2
$1.0 \times 10^{-9}$	15000	2.8	0.2	2.8	0.2	2.6	0.2

Assuming  $a_{\min}=0.1 \mu\text{m}$  and  $a_{\max} = 1000 \mu\text{m}$  for the inner disk (similar to that of the outer disk, except for  $a_{\min}$  that is slightly larger to avoid the presence of a strong  $10 \mu\text{m}$  silicate feature), and an inner disk extending from 0.2 to 30 AU, a dust mass in the inner disk of  $1 \times 10^{-7} M_{\odot}$  astronomical silicates reproduces the dip in the SED at  $15 \mu\text{m}$  and generates a flux of 1.6 mJy at  $870 \mu\text{m}$  inside 30 AU. The disk model convolved with a  $34 \times 70$  AU beam produces 6.7 mJy of continuum flux centered on the star, a flux below the  $3\sigma$  upper limit of the SMA observations. Using this dust mass, we found that gas-to-dust ratios between 100 and 200 can describe the CO P(10) line profile for a surface density power law exponent of 0.2. Lower gas masses in the inner disk (i.e. lower gas-to-dust ratios) generate too narrow CO P(10) profiles, higher gas masses (i.e. higher gas-to-dust ratios) produce line profiles with high-velocity wings too broad to be compatible with the observations. The best fit was achieved with a gas-to-dust ratio of 150, therefore, a gas mass inside the cavity of  $1.5 \times 10^{-5} M_{\odot}$ .

There is a degeneracy between the gas mass of the inner disk and the exponent of the power-law of the surface density. By increasing the power law exponent higher gas masses in the inner disk are allowed while reproducing the CO ro-vibrational line profile. However, there is an upper-bound to the gas mass in the inner disk if the condition that the surface density of the inner disk should be equal or lower than the surface density of the outer disk at 30 AU and that the flux of the [O I] line at  $63 \mu\text{m}$  should be reproduced. We found that up to  $10^{-4} M_{\odot}$  of gas are possible in the inner disk.

An alternative way of exploring the gas-to-dust ratio in the inner disk is to leave constant the gas mass and surface density and to decrease the dust mass in the silicate disk at  $0.2 < R < 30$

AU. In Fig. 9 we display the expected CO P(10) line profiles for Model 5, keeping the inner disk's gas mass constant ( $1.5 \times 10^{-5} M_{\odot}$ ) and decreasing the amount of dust down to a factor 100 (i.e. gas-to-dust ratios from 150 up to 15000). We found, that if the gas surface density inside the cavity is constant, a lower (astronomical silicates) dust mass does not affect significantly the CO  $4.7 \mu\text{m}$  profile and line flux, nor the flux of the [O I]  $63 \mu\text{m}$  line. A lower silicate dust mass inside the cavity lead to weaker emission in the  $5\text{--}10 \mu\text{m}$  band. However, as the SED near-IR emission is dominated by the carbon grains in the inner most disk, the SED fit is still compatible with the observations. The lower bound to the dust mass inside the cavity it is not constrained by current observations. To constrain the dust mass inside the cavity, observations at high spatial resolution are required, for example with ALMA. In Table 6 we provide prediction of the continuum fluxes at 430 and  $870 \mu\text{m}$  inside 30 AU for different silicate dust sizes and masses in Model 5.

### 5.6. Outer radius of the inner disk

In the family of Models 5, the inner disk has gas up to 30 AU. We have tested models with outer radius of the inner disk ranging from 15 to 30 AU. Solutions to the CO ro-vibrational line-profile can be found with a similar gas mass as Model 5, by allowing for a more positive exponent of the power law of the surface density distribution. For example for  $R_{\text{out}} = 15$  AU,  $q$  increases to +0.8. Models with an inner disk outer radius smaller than 30 AU produce slightly better fits to the top of the CO ro-vibrational line, however, they produce lower spectro-astrometry signatures and generate a surface density in the inner disk's outer radius slightly higher than the surface density at the outer disk's inner

radius. Current data do not allow-us to set the exact value of the outer radius of the inner disk. We favor a model with a cavity replenished with gas up to 30 AU because it generates a larger spectro-astrometry signature (although even with  $R_{\text{out}}=30$  AU, the spectro-astrometry signature is under predicted) and because surface densities with power-law exponents larger than 0.5 might result in a unstable disk. In summary, the presence of a gap in the gas of a few AU *in the gas* is consistent with the current data, a large gap of tens of AU appears not likely.

## 6. Discussion

### 6.1. The disk gas structure of HD 135344B and the origin of transition disk shape.

The growing observational evidence indicates that the gaps suggested by the SEDs and spatially resolved sub-mm observations are in fact structures that reflect the distribution of large grains, but not necessarily the distribution of small dust, and, especially the gas.

As noted by Pontoppidan et al. (2008) the presence of gas in the cavities disfavors photoevaporation as the possible origin of the transition disk shape in HD 135344B. A gas-to-dust ratio larger than 100 in the inner disk indicates that the mechanism depleting the material in the cavity is more efficient at depleting dust than the gas. This could potentially favor the grain-growth scenario. But, as noted by Birnstiel et al. (2012), grain-growth alone has difficulties to explain the lack of sub-mm emission in the gap.

Positive and flat power law surface density profiles ( $q=0$  and 1) for the inner disk of transition disks have previously suggested by Dong et al. (2012) in the frame of their general disk model to explain the H-band scattered light present inside the sub-mm dust cavities. Our results on the modeling of the CO ro-vibrational lines in HD 135344B provide an independent argument suggesting that the surface density profile inside the cavity can increase with radius in transition disks.

What implications has a positive surface density profile? In most protoplanetary disks the surface density distribution can be described by a power law with a negative exponent, typically -1.0 (i.e. a surface density that *decreases* with radius). A surface density profile with a positive power law exponent (or at least flat), indicates that the disk's gas structure has *significantly* changed in the inner disk. It is not entirely clear what mechanism will generate a surface density increasing with radius.

One interesting possibility is that indeed we are observing the effects of a jovian planet inside the inner cavity. Although the exact results of simulations depend on the inner boundary conditions set, for example the accretion rate onto the star, and the evolution time of the simulation, models studying the interaction of a jovian planet and the disk show that a disk with an initial negative power law surface density profile exponent could evolve into a disk which has a flat or a positive power law surface density profile exponent at  $R < R_{\text{planet}}$  (see for example Fig. 2 in Lubow & D'Angelo (2006), or Fig. 1 in Varnière et al. (2006) or Fig. 5 in Tatulli et al. (2011)). Furthermore, a single jovian planet is expected to open a gap typically of few AU width (see review by Kley & Nelson 2012). Such a small gap is compatible with current data and models of HD 135344B. Another predicted effect of the presence of a planet in the disk is a higher surface density for the gas in the outer disk with respect to the surface density for the gas in inner disk. We retrieve such gas surface density structure in our models, although, we find a surface

density difference that is smaller than that found by migration calculations (e.g., Lubow & D'Angelo 2006).

Taking all together, the characteristics found in HD 135344B evoke the effects of a migrating jovian planet present in the disk. However, at the present time there is no firm evidence for such a companion. Our models disfavor the presence of gaps of tens of AU in the gas inside the cavity of HD 135344B, therefore, disfavors the hypothesis that a multi-jovian planet system (e.g. Zhu et al. 2011; Dodson-Robinson & Salyk 2011) is the responsible of the transitional disk shape in HD 135344B. This conclusion could be extended to other accreting “pre-transitional” disks with CO ro-vibrational emission extending tens of AU, or with CO emission sub-mm emission inside the cavity.

Finally, the result that globally the amount of gas in the disk of HD 135344B (a few  $10^{-3} M_{\odot}$ ) is much lower than expected for a gas-to-dust ratio 100 indicates that HD 135344B is an evolved protoplanetary disk that that has already lost a large fraction of its gas mass. A low gas-to-dust has been reported for another transition disk IRS 48 (Bruderer et al. 2013). Further detailed studies in a larger sample of objects are required to test whether a lower gas mass is a common characteristic of the transition disk population.

### 6.2. Sublimation of dust grains in the inner disk, carbon grains, and optically thick “inner walls” in “pre-transitional” disks

One crucial ingredient for the simultaneous fitting of the SED and the CO 4.7  $\mu\text{m}$  emission extending tens of AU is the hypothesis of an inner most disk ( $R < 0.25$  AU) enriched with carbonaceous grains. This feature is essential to make possible to the CO warm gas at tens of AU to contribute to the CO P(10) line profile while having an inner disk that reproduces the near-IR SED.

The VLTI/PIONIER data clearly shows that the H-band excess is located inside 0.16 to 0.20 AU, the silicate sublimation radius of HD 135344B (the exact value depends on the mass of dust and  $n_{\text{H}}$ ). This provided a plausible physical explanation to the carbon enrichment in the inner-most disk: *carbon grains are present at  $0.08 < R < 0.2$  AU because silicate grains have sublimated*. The mass of carbonaceous grains required to fit the SED and the near-IR visibilities is  $2.5 \times 10^{-12} M_{\odot}$ . A small amount of dust when compared to the total dust mass of the disk that is around  $10^{-4} M_{\odot}$  and the dust mass at  $R < 30$  AU that is  $10^{-9}$  to  $10^{-7} M_{\odot}$ . In Model 5, the carbon abundance relative to  $n_{\text{H}}$  required in carbon grains is around two-times the solar abundance.

We have assumed that the size distribution of the carbonaceous grains in the inner-most disk is 0.1 to 10  $\mu\text{m}$ . Future detailed work of the process of dust evaporation in the inner disk of HD 135344B, for example as performed in the inner rim of Herbig Ae stars by Kama et al. (2009), or in the warm debris disk of Formalhaut by Lebreton et al. (2013), including the effects of gas would be required to constrain with a physical basis the dust size distribution of carbon and silicates as a function of the radius in the inner 1 AU of HD 135344B.

The presence of carbonaceous grains in inner disks to fit near-IR visibilities has been suggested in a few circumstellar disks. For example Absil et al. (2006) and Lebreton et al. (2013) in the cases of the warm debris disks of Vega and Formalhaut. Kraus et al. (2013) analyzed the (pre-) transitional disk V1247 Ori, a source relatively similar to HD 135344B. To fit V1247 Ori near-IR and mid-IR interferometry data, Kraus et al. have suggested a disk structure on which the inner-most disk is composed of a mixture of carbon (50%) and silicate (50%) grains at  $0.19 < R < 0.34$  AU, and a mass of  $10^{-7} M_{\odot}$  car-



bon dust grains inside  $0.3 < R < 46$  AU. The gap composed of carbon was suggested to avoid the presence of the  $10 \mu\text{m}$  silicate feature and also avoid a strong excess at  $\lambda > 8 \mu\text{m}$ . Furthermore, Kraus et al. have suggested the presence of some inhomogeneities in the “gap” material. At the time of writing there are no observations of CO ro-vibrational emission for V1247 Ori. In our model of HD 135344B, we ruled out a large fraction of carbon grains ( $>25\%$ ) at  $0.2 < R < 30$  AU on the basis of the CO ro-vibrational profile. A gap with a large fraction of carbon grains produces a narrow single peaked CO ro-vibrational line profile as the CO emission is dominated by the inner rim of the outer disk (see Model 2).

The carbonaceous grains inner-most disk inside the silicate sublimation radius proposed here for HD 135344B provides an alternative disk structure to the “optically thick-wall” suggested for “pre-transitional” disks (e.g., Espaillat et al. 2007, 2010; Brown et al. 2007). We have shown here that the “optically thick wall disk structure” is *not* compatible with the detection of CO ro-vibrational emission extending tens of AU. Therefore, the carbon-rich (or refractory grains rich) inner disk structure suggested for HD 135344B might be applicable other transition disks displaying near-IR excess and CO  $4.7 \mu\text{m}$  emission extending several AU (e.g., SR 21, Pontoppidan et al. 2008). Further near-IR interferometry observations of (pre-) transition disks are required to establish what fraction of them have dust material inside the silicates sublimation radius. Moreover, as in several transition and pre-transitional disks CO ro-vibrational emission has been detected (e.g., Pontoppidan et al. 2008; Salyk et al. 2009), it would be of great interest to extend the analysis presented here to them.

The models described here have used amorphous carbon grains. We have tested graphite grains using a mixture of 50% parallel and 50% perpendicular opacities. The fit to the CO P(10) line profile did not change significantly. The SED displayed a slightly weaker emission at  $3 - 10 \mu\text{m}$ .

A potential challenge for the presence of carbonaceous grains in the inner-most disk ( $0.08 < R < 0.2$  AU) is an oxygen rich atmosphere. Carbon grains would react with the oxygen and be destroyed (see for example the models of Gail 2001; Lee et al. 2010). The presence of carbon grains in the inner-most disk depends on the balance between the destruction and the replenishment time-scales.

To estimate the destruction time-scale by oxygen atoms (i.e. chemical sputtering), let us take one carbon grain of density  $\rho$ , initial size  $a_0$  and radius  $a$ . Atomic oxygen reacts with individual carbon atoms at the surface of the carbon grain, producing a change on the carbon grain’s size with time (Evans 1994):

$$\frac{\Delta a}{\Delta t} = \frac{a_0}{t} \simeq \dot{a} = -\frac{n_{\text{O}} m_{\text{C}} Y}{\rho} \left( \frac{k T_{\text{gas}}}{2\pi m_{\text{O}}} \right)^{1/2}, \quad (2)$$

here  $t$  is the time for the grain to be destroyed,  $n_{\text{O}}$  is the number density of Oxygen ( $n_{\text{O}} = n_{\text{H}} \chi_{\text{O}}$  and  $\chi_{\text{O}} = 3 \times 10^{-4}$ ),  $Y$  is the yield of this Eley-Rideal type reaction,  $k$  is the Boltzmann constant, and  $m_{\text{O}}$  is the mass of the Oxygen atom ( $m_{\text{O}} = 16 \times m_{\text{H}}$ ). Here we assume that the destruction rate is constant. Solving for  $t$  we obtain:

$$t \sim a_0 \frac{\rho}{n_{\text{O}} m_{\text{C}} Y} \left( \frac{2\pi m_{\text{O}}}{k T_{\text{gas}}} \right)^{1/2} \quad (3)$$

If the grain’s mass density  $\rho$  is  $2.2 \text{ g cm}^{-3}$ , then the lifetime of a carbon grain of radius  $a_0$  is

$$t \sim 0.28 \times \left( \frac{0.1}{Y} \right) \left( \frac{a_0}{0.01 \mu\text{m}} \right) \left( \frac{2000 \text{ K}}{T_{\text{gas}}} \right)^{1/2} \left( \frac{10^{10} \text{ cm}^{-3}}{n_{\text{H}}} \right) \text{ yr}. \quad (4)$$

The value of the yield is the not well constrained, assuming  $Y = 0.1$  (Vierbaum & Roth 2002, but it can be lower),  $n_{\text{H}} = 2 \times 10^{10} \text{ cm}^{-3}$  (mid-plane value at 0.1 AU in Model 5, see Fig. A.4 in the Appendix), this simple calculation shows that carbon grains with sizes 0.01, 0.1, and  $1 \mu\text{m}$  survive at 2000 K time scales around a month, a year, and ten years respectively.

To calculate the carbon replenishment time-scale at  $R < 0.2$  AU three input parameters are needed: the gas mass accretion rate, the gas-to-dust ratio, and the fraction in mass of dust grains in the form of carbonaceous grains at  $R > 0.2$  AU. Sitko et al. (2012) suggest a gas accretion rate of  $2 \times 10^{-8} M_{\odot}/\text{yr}$ . Our model indicate that the gas-to-dust ratio at  $R < 30$  AU is 150 (it can be larger). The mass fraction of carbon grains with respect to silicates at  $0.2 < R < 30$  AU can be constrained observationally, by the maximum mass of carbon that can be added and still keep the fit to the SED and the CO ro-vibrational line. We have found that up to 3% of the dust mass ( $10^{-9} M_{\odot}$ ) at  $0.2 < R < 30$  AU can be in the form of carbon grains and still fit the SED and CO lines. Taking together gas accretion rate, the gas-to-dust ratio, and the fraction in mass of carbon, we obtain a supply rate of carbon-grains to the inner-most disk of  $4 \times 10^{-12} M_{\odot}/\text{yr}$ . The life time of carbon grains larger than  $0.1 \mu\text{m}$  is years, thus, the disk can have of the order  $10^{-12} M_{\odot}$  transient carbon grains at  $R < 0.2$  AU. A carbon mass similar to that required to fit the near-IR SED in our models.

In summary, taking together the supply rate via dust mass accretion and the destruction timescales in the innermost disk, we find that a carbon inner-most ( $R < 0.2$  AU) disk could be indeed plausible in HD 135344B.

In a recent work, Lee et al. (2010) studied the survival of carbon grains in a T Tauri disk. Lee et al. find that carbon grains can be destroyed by oxygen atoms in the warm ( $T \sim 500$  K) upper layers of the disk in time scales ranging from tens to thousands of years depending on the carbon grain size, porosity, and distance of the star. The potential destruction of carbon grains at  $R > 0.2$  AU could present a challenge to the interpretation presented here. Lee et al. models are not dynamical models in the sense that the dust components are not followed with the gas in a simulation. Thus, it is unknown what fraction of the total amount of carbon grains will effectively reach the upper layers of the disk and be destroyed, what fraction of the carbon grains will survive in the mid-plane, and with what rate carbon grains at a few AU disk are replenished by the outer disk in an accreting disk. Future more detailed models including the dynamics of the gas, the interaction between the gas and the dust, the photochemistry of the disk, and carbon destruction would be of great help to further test the scenario proposed here.

From the point of view of the interpretation of the observations, other refractory grains in the inner-most disk, such as titanium, calcium, or aluminum bearing minerals (e.g. titanium or aluminum oxide) could be responsible for the near-IR excess observed. Since the current data do not constrain the inner disk composition to such degree of refinement (i.e. multiple refractory dust species), we did not attempt to fit our data with mixtures of carbon and/or other refractory components. We retained the amorphous carbon solution as it is the simplest refractory grain that can be assumed.

The conclusion that the inner-most disk of HD 135344B could be carbon-rich potentially presents a problem in a wider cosmochemical context, as the Earth and other terrestrial planets (as well as some exoplanetary systems, e.g. Xu et al. 2013) display a carbon to silicon deficit in comparison with meteorites, the Sun and the Interstellar Medium. Perhaps, HD 135344B is an unique object, or the processes responsible for the carbon deple-

tion on Earth are particular to the Solar System, or perhaps, there is much larger variety on the possible chemical compositions that terrestrial planets can have in different planetary systems. We stress that the carbon rich inner-most disk of HD 135344B is a plausible solution that allow-us to reproduce simultaneously all available gas and dust observables of the inner disk, most notably the near IR visibilities indicating continuum emission inside the silicate sublimation radius, and the CO ro-vibrational emission extending tens of AU, but that other refractory grains could provide similar solutions. Amorphous carbon grains provide the simplest solution that fit the data, but, they are not the only possible solution.

### 6.3. Double and single peaked CO-rovibrational line profiles in transition disks

In a recent study of CO-rovibrational emission in young stars Bast et al. (2011) have observed three types of line profiles: (1) double-peaked, (2) narrow-single peaked, and (3) single peaked with broad base. Bast et al. argue that the profiles of type 3 originate from a combination of emission from the inner part of the disk ( $R < a$  few AU), and emission from a slow moving disk wind. In their analysis Bast et al. suggest line profile parameter  $P_{10}$  (the full width line profile at 10% of its height divided by the full width of the line profile at 90%) to distinguish between the different types of line profiles. In the case of HD 135344B, the value of  $P_{10}$ , obtained from an average of the lower J-transition lines up to P(14), is 6.9. Thereby locating HD 135344B just above the value of 6, the maximum line profile parameter for a Keplerian disk model with a power-law temperature profile.

In our models of HD 135344B, we have found that the CO ro-vibrational line profile is the result of the combination of two contributions: (1) the emission from the gas inside the dust cavity and (2) the emission from the gas located in the inner rim of the outer disk. The relative contribution of both components, thus, the CO ro-vibrational line profile, depends on the properties of the dust in the inner disk and the gas mass in the inner and outer disk.

In Models 1 and 2, we have shown the effect of the inner disk dust composition on the CO ro-vibrational line profile. If the optical of the continuum at  $4.7 \mu\text{m}$  inside 30 AU is small ( $\tau < 0.1$ , e.g. Model 2), then the CO ro-vibrational emission will be dominated by the contribution of the inner-rim of the outer disk and a narrow single peaked line profile would be produced.

A single peaked line profile can also be obtained by increasing the gas mass in the outer disk, or diminishing the gas mass in the inner disk, or increasing the scale-height of the outer disk with respect to the inner disk. In the case of Model 5, if the gas mass in the outer disk is increased such that the gas-to-dust ratio is larger than 10, then the line profile becomes more and more single peaked (see bottom panel of Fig. 8).

In summary, our radiative transfer calculations of the CO  $4.7 \mu\text{m}$  emission show that in the case of transition disks, the presence of single peaked CO ro-vibrational line profiles can be explained by Keplerian disk emission without the recourse of a disk wind component. Note that this only applies for sources in which the emission line center is not blue-shifted with respect to the stellar velocity.

## 7. Summary and Conclusion

We have conducted a modeling effort aimed at constraining the gas mass and the gas and dust disk structure of the transition

disk HD 135344B from multi-instrument and multi-wavelength observations of gas and dust.

We have found that the previously suggested inner disk structure (Brown et al. 2007), namely a narrow dust inner disk of from 0.18 to 0.45 AU followed by a large 45 AU dust gap replenished with gas, fails to reproduce the CO ro-vibrational emission observed as the line profile produced from this disk model is a broad double peak.

We have found a disk model that is able to reproduce current observational constraints. This disk is composed of three zones:

1. A first zone between 0.08 and 0.2 AU composed of small carbonaceous grains (and gas) with a total dust mass of a few  $10^{-12} M_{\odot}$  (a few solar abundances of carbon). The presence of this inner carbonaceous grains provides:
  - a) A fit to the near-IR H-band visibilities and closure phases.
  - b) A fit of the near-IR SED while allowing the warm CO at several AU to emit and contribute to the  $4.7 \mu\text{m}$  line profile.
  - c) An agreement with the higher temperatures ( $T > 1500$  K) expected in this zone.
2. A second zone extending from 0.2 to 30 AU (i.e. the dust cavity) replenished with gas ( $10^{-5}$ - $10^{-4} M_{\odot}$ ) with a surface density increasing as a function of the radius and dust mass of astronomical silicates of maximum  $10^{-7} M_{\odot}$ . An increasing surface density profile is required to fit the shape of the CO ro-vibrational emission lines. The fit to the SED constrain the scale height between 0.09 and 0.13 at 10 AU with a flaring exponent 1.12. The gas-to-dust ratio in this zone is larger 100, however, the exact value is not well constrained. We found models up to gas-to-dust ratios 15 000 consistent with the observations either by decreasing the silicate dust mass a factor 100, or by increasing the gas mass a factor of a few and a higher power law exponent of the surface density distribution. The upper bound to the gas mass at  $R < 30$  AU is given by the flux of the [O I]  $63 \mu\text{m}$  combined with the requirement that the surface density of the inner disk should be equal or lower than the surface density of the outer disk at 30 AU. The dust surface density at  $R < 30$  AU is lower than the one expected from extrapolating the dust surface density from the outer disk. This zone can contain up to a 3% in mass ( $\sim 10^{-9} M_{\odot}$ ) in carbon grains and keep the fit to the SED.
3. A third zone from 30 AU to 200 AU (the outer disk) with astronomical silicate grains, a dust mass of  $2 \times 10^{-4} M_{\odot}$ , a gas mass  $10^{-4} - 10^{-3} M_{\odot}$  (gas-to-dust ratio  $< 10$ ), surface density exponent of -1.0, and flaring 1.0. In this zone large ( $0.1 < a < 1000 \mu\text{m}$ ) and small ( $0.1 < a < 10 \mu\text{m}$ ) dust grains have different radial and vertical spatial distributions. Large grains are located at  $45 < R < 200$  AU in a disk with scale height 0.05 and 75% of the gas and dust mass. Small grains are located at  $30 < R < 200$  AU in a disk with higher scale height (0.09 to 0.13, i.e., the same H/R as zone 2) and 25% of the gas and dust mass. The vertical structure of the outer disk echoes the expected effects of dust growth and settling. A gas-to-dust ratio much lower than 100 in the outer disk is required to fit the [O I]  $63 \mu\text{m}$  line flux and to reproduce the CO ro-vibrational line profile simultaneously.

The models suggest that the best fit to the gas observations in HD 135344B is provided by a disk in which the gas surface density and the scale height have no large discontinuities at 30 and 45 AU. In other words that there is no large gap in the gas distribution of HD 135344B. The cavity observed in the near-IR

and sub-mm is replenished by gas and (some) dust. The presence of a small gap of a few AU in the gas is consistent with current data, a large gap in the gas of tens of AU appears not likely.

The global gas-to-dust ratio, i.e. integrated over the full disk, is much lower than 100. This provides further evidence that HD 135344B is an evolved protoplanetary disk that has already lost a large fraction of its gas mass.

The disk structure proposed for HD 135344B could be applied to other “pre-transitional” disks with CO ro-vibrational emission extending to several AU.

The increasing surface density profile of the gas in the inner disk, the difference in the radial distribution of large and small grains in the outer disk, and a small gap in the gas between the inner and outer disk are compatible with the dynamical interaction of a single jovian planet and the disk. However, we should be cautious as other mechanisms could be responsible of the gas and dust distribution observed in HD 135344B.

The current ensemble of observations show the transitional disk features (i.e. gap) observed in the continuum reflect only changes on the distribution of large and small dust particles in the disk. The gas has a spatial distribution that can differ from that of the dust, particularly that of large grains observed in the sub-mm. Furthermore, we find that the gas distribution and mass in transition disks can be very different to that of primordial disks.

Our modeling results predict that gas and (some) dust emission should be detected inside the cavity with high-sensitivity and high-spatial resolution sub-mm observations. ALMA measurements of continuum emission inside 30 AU would be of great help in determining the dust size distribution and dust mass inside the cavity, quantities that at the present are free parameters in the model. ALMA gas observations at high spatial resolution, for example the CO 6-5 line, used in conjunction with other gas tracers will allow to better constrain the gas mass inside cavity, and the gas mass and surface density in the outer disk.

Future detailed dynamical disk models including the dynamics of the gas, the interaction between the gas and the dust, the photo-chemistry of the disk, and carbon destruction would be of great help to establish whether the carbon inner-most disk suggested our modeling is viable, or whether the inclusion refractory grains different than carbon is necessary.

In this paper we showed that the simultaneous modeling of gas and dust observations is required to address the problem of the dust and gas structure of protoplanetary disks.

**Acknowledgements.** A. Carmona and C. Pinte acknowledge funding from the European Commission’s 7<sup>th</sup> Framework Program (EC-FP7) (contract PERG06-GA-2009-256513) and from Agence Nationale pour la Recherche (ANR) of France under contract ANR-2010-JCJC-0504-01. Calculations were performed at Service Commun de Calcul Intensif de l’Observatoire de Grenoble (SCCI) on the Fostino super-computer funded by ANR (contracts ANR-07-BLAN-0221, ANR-2010-JCJC-0504-01 and ANR-2010-JCJC-0501-01) and the EC-FP7 contract PERG06-GA-2009-256513. The research leading to these results has received funding from the EC-FP7 under grant agreement no 284405. FMe acknowledges support from the Millennium Science Initiative (Chilean Ministry of Economy), through grant Nucleus P10-022-F. PIONIER is funded by the Université Joseph Fourier (UJF), the Institut de Planétologie et d’Astrophysique de Grenoble (IPAG), the Agence Nationale pour la Recherche (ANR-06-BLAN-0421 and ANR-10-BLAN-0505), and the Institut National des Sciences de l’Univers (INSU PNP and PNPS). The integrated optics beam combiner is the result of a collaboration between IPAG and CEA-LETI based on CNES R&T funding. Part of this work was funded by the Agence National pour la Recherche of France through the Chaire d’Excellence grant ANR (CHEX2011 SEED). This research has made use of the SIMBAD database, operated at CDS, Strasbourg, France. This work is based [in part] on archival data obtained with the Spitzer Space Telescope, which is operated by the Jet Propulsion Laboratory, California Institute of Technology under a contract with NASA. We thank Alex Brown for providing the Chandra X-ray luminosity.

## References

- Absil, O., di Folco, E., Mérand, A., et al. 2006, *A&A*, 452, 237  
 Alexander, R. D. & Armitage, P. J. 2007, *MNRAS*, 375, 500  
 Andrews, S. M., Wilner, D. J., Espaillat, C., et al. 2011, *ApJ*, 732, 42  
 Bast, J. E., Brown, J. M., Herczeg, G. J., van Dishoeck, E. F., & Pontoppidan, K. M. 2011, *A&A*, 527, A119  
 Bertone, E., Buzzoni, A., Chávez, M., & Rodríguez-Merino, L. H. 2008, *A&A*, 485, 823  
 Birnstiel, T., Andrews, S. M., & Ercolano, B. 2012, *A&A*, 544, A79  
 Bouwman, J., Henning, T., Hillenbrand, L. A., et al. 2008, *ApJ*, 683, 479  
 Brown, J. M., Blake, G. A., Dullemond, C. P., et al. 2007, *ApJ*, 664, L107  
 Brown, J. M., Blake, G. A., Qi, C., et al. 2009, *ApJ*, 704, 496  
 Bruderer, S., van der Marel, N., van Dishoeck, E. F., & van Kempen, T. A. 2013, *ArXiv e-prints*  
 Calvet, N., D’Alessio, P., Watson, D. M., et al. 2005, *ApJ*, 630, L185  
 Cardelli, J. A., Clayton, G. C., & Mathis, J. S. 1989, *ApJ*, 345, 245  
 Carmona, A., van den Ancker, M. E., Audard, M., et al. 2010, *A&A*, 517, A67  
 Carmona, A., van der Plas, G., van den Ancker, M. E., et al. 2011, *A&A*, 533, A39  
 Casassus, S., van der Plas, G., M., S. P., et al. 2013, *Nature*, 493, 191  
 Chiang, E. & Murray-Clay, R. 2007, *Nature Physics*, 3, 604  
 Cieza, L., Padgett, D. L., Stapelfeldt, K. R., et al. 2007, *ApJ*, 667, 308  
 Cieza, L. A., Schreiber, M. R., Romero, G. A., et al. 2010, *ApJ*, 712, 925  
 Cieza, L. A., Schreiber, M. R., Romero, G. A., et al. 2012, *ApJ*, 750, 157  
 Coulson, I. M. & Walthers, D. M. 1995, *MNRAS*, 274, 977  
 Currie, T. & Sicilia-Aguilar, A. 2011, *ApJ*, 732, 24  
 Damjanov, I., Jayawardhana, R., Scholz, A., et al. 2007, *ApJ*, 670, 1337  
 Dent, W. R. F., Greaves, J. S., & Coulson, I. M. 2005, *MNRAS*, 359, 663  
 Dodson-Robinson, S. E. & Salyk, C. 2011, *ApJ*, 738, 131  
 Dong, R., Rafikov, R., Zhu, Z., et al. 2012, *ApJ*, 750, 161  
 Doucet, C., Pantin, E., Lagage, P. O., & Dullemond, C. P. 2006, *A&A*, 460, 117  
 Draine, B. T. & Lee, H. M. 1984, *ApJ*, 285, 89  
 Dullemond, C. P. & Dominik, C. 2005, *A&A*, 434, 971  
 Dunkin, S. K., Barlow, M. J., & Ryan, S. G. 1997, *MNRAS*, 286, 604  
 Espaillat, C., Calvet, N., D’Alessio, P., et al. 2007, *ApJ*, 670, L135  
 Espaillat, C., D’Alessio, P., Hernández, J., et al. 2010, *ApJ*, 717, 441  
 Evans, A. 1994, *The dusty universe*  
 Fang, M., van Boekel, R., Wang, W., et al. 2009, *A&A*, 504, 461  
 Fedele, D., Bruderer, S., van Dishoeck, E. F., et al. 2013, *ArXiv e-prints*  
 Fedele, D., van den Ancker, M. E., Acke, B., et al. 2008, *A&A*, 491, 809  
 France, K., Schindhelm, E., Herczeg, G. J., et al. 2012, *ApJ*, 756, 171  
 Gail, H.-P. 2001, *A&A*, 378, 192  
 Garufi, A., Quanz, S. P., Avenhaus, H., et al. 2013, *ArXiv e-prints*  
 Geers, V. C., Augereau, J.-C., Pontoppidan, K. M., et al. 2006, *A&A*, 459, 545  
 Grady, C. A., Schneider, G., Sitko, M. L., et al. 2009, *ApJ*, 699, 1822  
 Harvey, P. M., Smith, B. J., Difrancesco, J., Colome, C., & Low, F. J. 1996, *ApJ*, 471, 973  
 Helling, C., Oevermann, M., Lüttke, M. J. H., Klein, R., & Sedlmayr, E. 2001, *A&A*, 376, 194  
 Hernández, J., Briceño, C., Calvet, N., et al. 2006, *ApJ*, 652, 472  
 Hughes, A. M., Andrews, S. M., Espaillat, C., et al. 2009, *ApJ*, 698, 131  
 Isella, A., Pérez, L. M., & Carpenter, J. M. 2012, *ApJ*, 747, 136  
 Kama, M., Min, M., & Dominik, C. 2009, *A&A*, 506, 1199  
 Kamp, I. & Dullemond, C. P. 2004, *ApJ*, 615, 991  
 Kamp, I., Woitke, P., Pinte, C., et al. 2011, *A&A*, 532, A85  
 Kley, W. & Nelson, R. P. 2012, *ARA&A*, 50, 211  
 Kobayashi, H., Kimura, H., Watanabe, S.-i., Yamamoto, T., & Müller, S. 2011, *Earth, Planets, and Space*, 63, 1067  
 Kraus, S., Ireland, M. J., Sitko, M. L., et al. 2013, *ApJ*, 768, 80  
 Lahuis, F., van Dishoeck, E. F., Blake, G. A., et al. 2007, *ApJ*, 665, 492  
 Lahuis, F., van Dishoeck, E. F., Boogert, A. C. A., et al. 2006, *ApJ*, 636, L145  
 Laor, A. & Draine, B. T. 1993, *ApJ*, 402, 441  
 Lebreton, J., van Lieshout, R., Augereau, J.-C., et al. 2013, *ArXiv e-prints*  
 Lee, J.-E., Bergin, E. A., & Nomura, H. 2010, *ApJ*, 710, L21  
 Li, A. & Draine, B. T. 2001, *ApJ*, 554, 778  
 Li, A. & Greenberg, J. M. 1997, *A&A*, 323, 566  
 Lubow, S. H. & D’Angelo, G. 2006, *ApJ*, 641, 526  
 Lyo, A.-R., Ohashi, N., Qi, C., Wilner, D. J., & Su, Y.-N. 2011, *AJ*, 142, 151  
 Maaskant, K. M., Honda, M., Waters, L. B. F. M., et al. 2013, *ArXiv e-prints*  
 Mariñas, N., Telesco, C. M., Fisher, R. S., & Packham, C. 2011, *ApJ*, 737, 57  
 Meeus, G., Montesinos, B., Mendigutía, I., et al. 2012, *A&A*, 544, A78  
 Meeus, G., Salyk, C., Bruderer, S., et al. 2013, *ArXiv e-prints*  
 Merín, B., Brown, J. M., Oliveira, I., et al. 2010, *ApJ*, 718, 1200  
 Müller, A., van den Ancker, M. E., Launhardt, R., et al. 2011, *A&A*, 530, A85  
 Muto, T., Grady, C. A., Hashimoto, J., et al. 2012, *ApJ*, 748, L22  
 Muzerolle, J., Allen, L. E., Megeath, S. T., Hernández, J., & Gutermuth, R. A. 2010, *ApJ*, 708, 1107

- Najita, J. R., Carr, J. S., Glassgold, A. E., & Valenti, J. A. 2007a, *Protostars and Planets V*, 507
- Najita, J. R., Strom, S. E., & Muzerolle, J. 2007b, *MNRAS*, 378, 369
- Owen, J. E., Clarke, C. J., & Ercolano, B. 2012, *MNRAS*, 422, 1880
- Piétu, V., Dutrey, A., & Guilloteau, S. 2007, *A&A*, 467, 163
- Pinilla, P., Benisty, M., & Birnstiel, T. 2012, *A&A*, 545, A81
- Pinte, C., Harries, T. J., Min, M., et al. 2009, *A&A*, 498, 967
- Pinte, C., Ménard, F., Duchêne, G., & Bastien, P. 2006, *A&A*, 459, 797
- Pinte, C., Woitke, P., Ménard, F., et al. 2010, *A&A*, 518, L126
- Pontoppidan, K. M., Blake, G. A., van Dishoeck, E. F., et al. 2008, *ApJ*, 684, 1323
- Rebull, L. M., Padgett, D. L., McCabe, C.-E., et al. 2010, *ApJS*, 186, 259
- Rice, W. K. M., Armitage, P. J., Wood, K., & Lodato, G. 2006, *MNRAS*, 373, 1619
- Salyk, C., Blake, G. A., Boogert, A. C. A., & Brown, J. M. 2009, *ApJ*, 699, 330
- Sandell, G., Weintraub, D. A., & Hamidouche, M. 2011, *ApJ*, 727, 26
- Schindhelm, E., France, K., Burgh, E. B., et al. 2012, *ApJ*, 746, 97
- Schmidt-Kaler, T. 1982, in *Landolt-Boernstein: Numerical Data and Functional Relationships in Science and Technology. New Series*, Berlin: Springer, 1982, edited by Schaifers, K.; Voigt, H.H.; Landolt, Hans; Boernstein, Richard; Hellwege, K.H. (Editor-in-Chief) (Springer)
- Sicilia-Aguilar, A., Hartmann, L., Calvet, N., et al. 2006, *ApJ*, 638, 897
- Sitko, M. L., Day, A. N., Kimes, R. L., et al. 2012, *ApJ*, 745, 29
- Skrutskie, M. F., Cutri, R. M., Stiening, R., et al. 2006, *AJ*, 131, 1163
- Strom, K. M., Strom, S. E., Edwards, S., Cabrit, S., & Skrutskie, M. F. 1989, *AJ*, 97, 1451
- Sylvester, R. J., Skinner, C. J., Barlow, M. J., & Mannings, V. 1996, *MNRAS*, 279, 915
- Tatulli, E., Benisty, M., Ménard, F., et al. 2011, *A&A*, 531, A1
- Thi, W. F., Kamp, I., Woitke, P., et al. 2013, *A&A*, 551, A49
- Thi, W. F., van Dishoeck, E. F., Blake, G. A., et al. 2001, *ApJ*, 561, 1074
- van Boekel, R., Min, M., Waters, L. B. F. M., et al. 2005, *A&A*, 437, 189
- van der Plas, G., van den Ancker, M. E., Fedele, D., et al. 2008, *A&A*, 485, 487
- Varnière, P., Blackman, E. G., Frank, A., & Quillen, A. C. 2006, *ApJ*, 640, 1110
- Vicente, S., Merín, B., Hartung, M., et al. 2011, *A&A*, 533, A135
- Vierbaum, R. & Roth, P. 2002, *Proceedings of the Combustion Institute*, 29, 2423
- Walker, H. J. & Wolstencroft, R. D. 1988, *PASP*, 100, 1509
- Williams, J. P. & Cieza, L. A. 2011, *ARA&A*, 49, 67
- Woitke, P., Kamp, I., & Thi, W.-F. 2009, *A&A*, 501, 383
- Woitke, P., Pinte, C., Tilling, I., et al. 2010, *MNRAS*, 405, L26
- Xu, S., Jura, M., Klein, B., Koester, D., & Zuckerman, B. 2013, *ApJ*, 766, 132
- Zhu, Z., Nelson, R. P., Dong, R., Espaillat, C., & Hartmann, L. 2012, *ApJ*, 755, 6
- Zhu, Z., Nelson, R. P., Hartmann, L., Espaillat, C., & Calvet, N. 2011, *ApJ*, 729, 47

## Appendix A:

### A.1. Photometry

In this appendix, we summarize the different sources of the photometry used to construct the SED.

### A.2. Stellar Parameters

The stellar properties of HD 135344B have been studied by previous authors (e.g., Dunkin et al. 1997; Müller et al. 2011; Andrews et al. 2011). While authors agree on a spectral type F4, an effective temperature  $6750 \pm 150$  K (6660 K, Dunkin et al. 1997; 6590 K, Andrews et al. 2011;  $6810 \pm 80$  K, Müller et al. 2011), and a mass of 1.6 to 1.7  $M_{\odot}$ , there is a discrepancy on estimations of the radius of the star. Müller et al. (2011) suggest a radii of  $1.4 \pm 0.25 R_{\odot}$ , while Andrews et al. (2011) suggest a radii of  $2.15 R_{\odot}$ .

To have an independent assessment of the star properties, we downloaded reduced archival high-resolution ( $R=75\,000$ ) ESO/VLT-UVES spectra of HD 135344B in the 4800 to 5500 Å, and 5830 – 6800 Å range and used the interactive spectra visualization tool described in Carmona et al. (2010) to compare the UVES spectrum to BLUERED (Bertone et al. 2008) high-resolution synthetic spectra, in regions not contaminated

by emission lines or telluric absorption. We found that the optical spectra of HD 135344B is compatible spectral templates with  $T_{\text{eff}}$  ranging from 6500 to 7000 K for  $\log g$  ranging between 4.0 and 5.0 (see Fig. A.1). Naturally  $\log g = 5.0$  is not realistic as  $\log g = 4.33$  for a F-type star on the main sequence. The minimum in the  $\chi^2$  statistic suggest a  $T_{\text{eff}}$  around 6750 K.

To have a second constrain on the spectral type and  $A_V$  we employed the HST/COS<sup>6</sup> spectrum of HD 135344B. In Fig. A.2, we display coadded COS spectrum of HD 135344B, smoothed by a running 9 point boxcar filter, and de-reddened by a Cardelli et al. (1989)  $R=3.1$  extinction curve with  $E(B-V)=0.129$  ( $A_V=0.4$ ). We over-plot F3V (HR 9028, IUE SWP 14002, red) and F4V (HD 27901, SWP 45935, blue) spectral type comparison stars scaled by the difference in V magnitudes between them and HD 135344B. The spectral template F4V provides the best fit to the observed COS spectrum. The F4V spectrum corresponds to a  $T_{\text{eff}}$  6620 K using Schmidt-Kaler (1982).

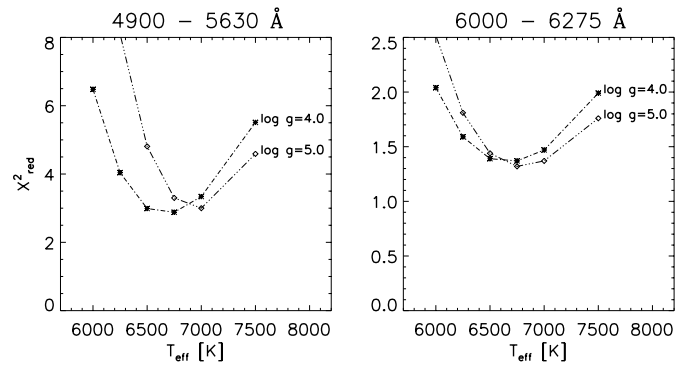


**Fig. A.1.**  $\chi^2_{\text{red}}$  as a function of the  $T_{\text{eff}}$  of the observed VLT/UVES high-resolution ( $R=75\,000$ ) spectrum and a rotational broadened BLUERED (Bertone et al. 2008) high-resolution synthetic spectra,  $v \sin i$  was set to minimize  $\chi^2_{\text{red}}$  for each  $T_{\text{eff}}$  and  $\log g$ .

To obtain an estimate of the luminosity and to constrain the value of the radius, we used a distance of 140 pc (van Boekel et al. 2005), the  $B$  and  $V$  photometry (9.2 and 8.7, SIMBAD database), and the  $T_{\text{eff}}$ ,  $M_V$ ,  $BC$  values of Schmidt-Kaler (1982) for stars of luminosity class V (i.e., smallest possible radii). We obtained that for a  $T_{\text{eff}}$  equal to 6440 K (F5) and 6890 K (F2)  $R=2.09$  and  $2.07 R_{\odot}$  respectively. Interpolating for  $T_{\text{eff}}$  6620 K, we obtained  $2.08 R_{\odot}$ . These values are closer to the radius estimate of  $2.15 R_{\odot}$  suggested by Andrews et al. (2011) than  $1.4 R_{\odot}$  claimed by Müller et al. (2011).

For our models, we used a star with  $T_{\text{eff}}=6620$  K (F4V), a stellar radius of  $2.1 R_{\odot}$ , a mass of  $1.65 M_{\odot}$  and  $A_V = 0.4$ .

<sup>6</sup> Cosmic Origins Spectrograph

**Table A.1.** Photometry

$\lambda$ [ $\mu\text{m}$ ]	$\lambda F_\lambda$ [ $\text{W m}^{-2}$ ]	Error [ $\text{W m}^{-2}$ ]	References	$\lambda$ [ $\mu\text{m}$ ]	$\lambda F_\lambda$ [ $\text{W m}^{-2}$ ]	Error [ $\text{W m}^{-2}$ ]	References
0.105	$2.8 \times 10^{-15}$	$1.6 \times 10^{-15}$	FUSE	10.70	$3.047 \times 10^{-13}$	$3.1 \times 10^{-16}$	Spitzer
0.110	$4.6 \times 10^{-15}$	$1.7 \times 10^{-15}$	FUSE	12.25	$2.038 \times 10^{-13}$	$2.8 \times 10^{-16}$	"
0.115	$5.1 \times 10^{-15}$	$1.9 \times 10^{-15}$	FUSE	14.03	$1.514 \times 10^{-13}$	$1.9 \times 10^{-16}$	"
0.118	$7.5 \times 10^{-15}$	$2.7 \times 10^{-15}$	FUSE	16.34	$2.047 \times 10^{-13}$	$2.3 \times 10^{-16}$	"
0.119	$3.7 \times 10^{-15}$	$3.7 \times 10^{-16}$	COS	19.39	$3.644 \times 10^{-13}$	$3.6 \times 10^{-16}$	"
0.123	$4.8 \times 10^{-15}$	$3.7 \times 10^{-16}$	COS	22.15	$4.955 \times 10^{-13}$	$4.2 \times 10^{-16}$	"
0.129	$3.6 \times 10^{-15}$	$3.2 \times 10^{-16}$	COS	25	$8.0 \times 10^{-13}$	$1.1 \times 10^{-13}$	IRAS <sup>b</sup>
0.137	$2.7 \times 10^{-15}$	$3.2 \times 10^{-16}$	COS	25.39	$6.280 \times 10^{-13}$	$5.8 \times 10^{-16}$	Spitzer
0.142	$2.2 \times 10^{-15}$	$1.3 \times 10^{-15}$	COS	29.73	$8.155 \times 10^{-13}$	$8.8 \times 10^{-16}$	"
0.152	$3.4 \times 10^{-15}$	$2.1 \times 10^{-15}$	COS	47	$1.5 \times 10^{-12}$	$2.2 \times 10^{-13}$	Harvey et al. (1996)
0.163	$7.6 \times 10^{-15}$	$6.6 \times 10^{-16}$	COS	60	$1.3 \times 10^{-12}$	$1.8 \times 10^{-13}$	IRAS <sup>b</sup>
0.169	$9.2 \times 10^{-15}$	$8.2 \times 10^{-16}$	COS	60	$1.4 \times 10^{-12}$	$2.0 \times 10^{-13}$	ISOPHOT
0.174	$1.4 \times 10^{-14}$	$1.1 \times 10^{-15}$	COS	63.18	$1.20 \times 10^{-12}$	$4.7 \times 10^{-15}$	GASPS
0.37	$3.4 \times 10^{-12}$	$1.6 \times 10^{-13}$	Coulson & Walther (1995)	72.85	$9.84 \times 10^{-13}$	$4.1 \times 10^{-15}$	"
0.44	$6.7 \times 10^{-12}$	$1.4 \times 10^{-13}$	"	79.36	$8.96 \times 10^{-13}$	$3.8 \times 10^{-15}$	"
0.55	$7.4 \times 10^{-12}$	$1.1 \times 10^{-13}$	"	80	$9.8 \times 10^{-13}$	$1.5 \times 10^{-13}$	ISOPHOT
0.65	$7.25 \times 10^{-12}$	$9.2 \times 10^{-14}$	"	89.99	$7.77 \times 10^{-13}$	$3.3 \times 10^{-15}$	GASPS
0.77	$5.3 \times 10^{-12}$	$1.2 \times 10^{-13}$	Grady et al. (2009)	90.16	$7.68 \times 10^{-13}$	$3.3 \times 10^{-15}$	"
0.8	$6.18 \times 10^{-12}$	$7.5 \times 10^{-14}$	Coulson & Walther (1995)	100	$6.9 \times 10^{-13}$	$1.2 \times 10^{-13}$	ISOPHOT
1.2	$4.5 \times 10^{-12}$	$1.0 \times 10^{-13}$	"	100	$7.7 \times 10^{-13}$	$7.7 \times 10^{-14}$	IRAS <sup>b</sup>
1.22	$4.80 \times 10^{-12}$	$9.8 \times 10^{-14}$	2MASS <sup>a</sup>	144.78	$3.97 \times 10^{-13}$	$2.1 \times 10^{-15}$	GASPS
1.6	$3.96 \times 10^{-12}$	$9.4 \times 10^{-14}$	Coulson & Walther (1995)	145.53	$3.96 \times 10^{-13}$	$2.1 \times 10^{-15}$	"
1.63	$4.4 \times 10^{-12}$	$1.3 \times 10^{-13}$	2MASS <sup>a</sup>	157.75	$3.78 \times 10^{-13}$	$1.9 \times 10^{-15}$	"
1.7	$4.1 \times 10^{-12}$	$1.8 \times 10^{-13}$	Grady et al. (2009)	179.52	$2.85 \times 10^{-13}$	$1.7 \times 10^{-15}$	"
2.19	$4.19 \times 10^{-12}$	$5.5 \times 10^{-14}$	2MASS <sup>a</sup>	180.42	$2.83 \times 10^{-13}$	$1.7 \times 10^{-15}$	"
2.2	$3.5 \times 10^{-12}$	$1.4 \times 10^{-13}$	Coulson & Walther (1995)	200	$1.4 \times 10^{-13}$	$1.0 \times 10^{-14}$	ISOPHOT
3.8	$2.10 \times 10^{-12}$	$7.9 \times 10^{-14}$	Coulson & Walther (1995)	350	$5.0 \times 10^{-14}$	$1.5 \times 10^{-14}$	Coulson & Walther (1995)
4.75	$1.48 \times 10^{-12}$	$6.3 \times 10^{-14}$	"	450	$2.5 \times 10^{-14}$	$1.0 \times 10^{-14}$	"
5.60	$1.681 \times 10^{-12}$	$1.2 \times 10^{-15}$	Spitzer	800	$2.4 \times 10^{-15}$	$1.5 \times 10^{-16}$	"
6.80	$1.083 \times 10^{-12}$	$8.8 \times 10^{-16}$	"	850	$1.73 \times 10^{-15}$	$3.5 \times 10^{-17}$	Sandell et al. (2011)
7.42	$8.949 \times 10^{-13}$	$8.2 \times 10^{-16}$	"	1100	$7.1 \times 10^{-16}$	$1.1 \times 10^{-16}$	Coulson & Walther (1995)
8.45	$6.565 \times 10^{-13}$	$7.1 \times 10^{-16}$	"	1300	$3.3 \times 10^{-16}$	$9.7 \times 10^{-17}$	Sylvester et al. (1996)
9.66	$4.965 \times 10^{-13}$	$5.2 \times 10^{-16}$	"				

**Notes.** <sup>(a)</sup> Skrutskie et al. (2006) <sup>(b)</sup> Walker & Wolstencroft (1988)

### A.3. CO 4.7 $\mu\text{m}$ emission

### A.4. Model 5: Herschel CO and water lines

### A.5. Details of Model 5

In this Appendix, we show additional plots of the structure and emitting regions of several gas tracers in Model 5.

**Table A.2.** Predicted and observed CO rotational emission line fluxes by Model 5 at Herschel, sub-mm, and mm wavelengths

Transition	$\lambda$ [ $\mu\text{m}$ ]	Flux [ $10^{-19} \text{ W m}^{-2}$ ]	Observed [ $10^{-19} \text{ W m}^{-2}$ ]	Ref.
$J = 36 - 35$	72.84	0.4	< 246	1
$J = 29 - 28$	90.16	1.7	< 191	1
$J = 23 - 22$	113.46	3.9	< 128	1
$J = 18 - 17$	144.78	5.5	< 69	1
$J = 15 - 14$	173.63	9.1	< 155	1
$J = 6 - 5$	433.55	8.3	...	
$J = 5 - 4$	520.23	5.6	...	
$J = 4 - 3$	650.25	3.3	...	
$J = 3 - 2$	866.96	1.5	1.2	2
$J = 2 - 1$	1300.40	0.5	0.8	3
$J = 1 - 0$	2600.75	0.06	...	

**References:** (1) Meeus et al. (2013); (2) Dent et al. (2005); (3) Thi et al. (2001)

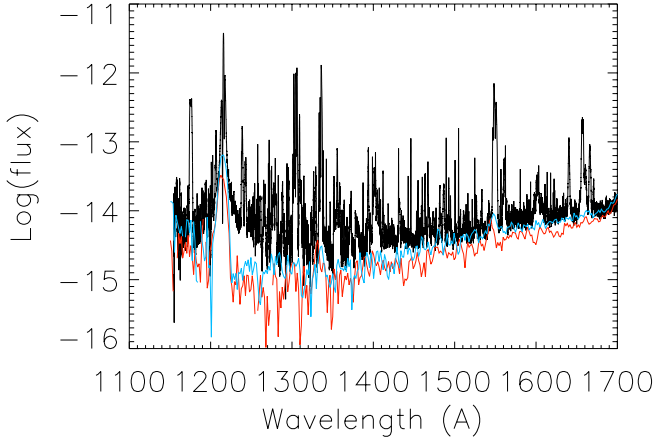


**Fig. A.2.** Coadded HST-COS spectrum of HD 135344B smoothed and de-reddened (see details in the text). F3V (HR 9028, IUE SWP 14002, red) and F4V (HD 27901, SWP 45935, blue) spectral type comparison stars are shown, scaled by the difference in V magnitudes between them and HD 135344B. HD 135344B shows a distinct FUV excess for wavelengths shortward of 1600 Å, demonstrating the accretion luminosity. The structure seen in the COS data is not noise, but fluorescent H<sub>2</sub> emission (France et al. 2012). The rise in flux for the comparison stars shortward of H I Lyman  $\alpha$  is an artifact. No correction in all of the spectra has been made for geocoronal Lyman  $\alpha$ .

**Table A.3.** Predicted rotational emission line fluxes by Model 5 in selected H<sub>2</sub>O water lines at Herschel wavelengths.

Transition	$\lambda$ [ $\mu$ m]	Flux [ $10^{-19}$ W m $^{-2}$ ]	Observed [ $10^{-19}$ W m $^{-2}$ ]	Ref.
o-H <sub>2</sub> O 8 <sub>18</sub> – 7 <sub>07</sub>	63.32	3.7	< 120	1
o-H <sub>2</sub> O 7 <sub>16</sub> – 6 <sub>25</sub>	66.09	2.8	< 120	1
o-H <sub>2</sub> O 3 <sub>30</sub> – 2 <sub>21</sub>	66.44	23.7	< 120	1
o-H <sub>2</sub> O 7 <sub>07</sub> – 6 <sub>16</sub>	71.96	7.8	< 120	1
o-H <sub>2</sub> O 3 <sub>21</sub> – 2 <sub>12</sub>	75.39	26.1	< 120	1
o-H <sub>2</sub> O 4 <sub>23</sub> – 3 <sub>12</sub>	78.74	19.6	< 120	1
o-H <sub>2</sub> O 6 <sub>16</sub> – 5 <sub>05</sub>	82.03	12.2	< 120	1
o-H <sub>2</sub> O 2 <sub>21</sub> – 1 <sub>10</sub>	108.07	18.8	< 120	1
o-H <sub>2</sub> O 3 <sub>03</sub> – 2 <sub>12</sub>	174.62	12.5	< 120	1
o-H <sub>2</sub> O 2 <sub>11</sub> – 1 <sub>01</sub>	179.53	16.6	< 120	1
p-H <sub>2</sub> O 7 <sub>26</sub> – 6 <sub>15</sub>	59.99	0.8	< 120	1
p-H <sub>2</sub> O 6 <sub>15</sub> – 5 <sub>24</sub>	78.93	1.0	< 120	1
p-H <sub>2</sub> O 6 <sub>06</sub> – 5 <sub>15</sub>	83.29	3.7	< 120	1
p-H <sub>2</sub> O 4 <sub>13</sub> – 4 <sub>04</sub>	187.11	1.0	< 120	1

**References:** (1) Upper limit at 145  $\mu$ m is assumed (Fedele et al. 2013);

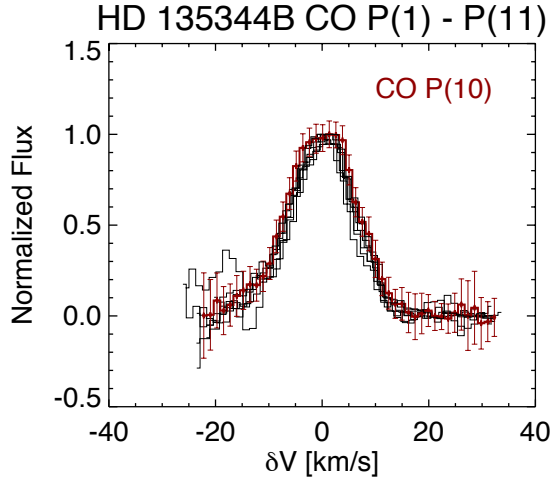


**Fig. A.3.** The CO P(1) to P(11) line profiles are available within the CRILES spectrum. The lines have been continuum subtracted and normalized by the peak flux. In red the CO P(10) line.



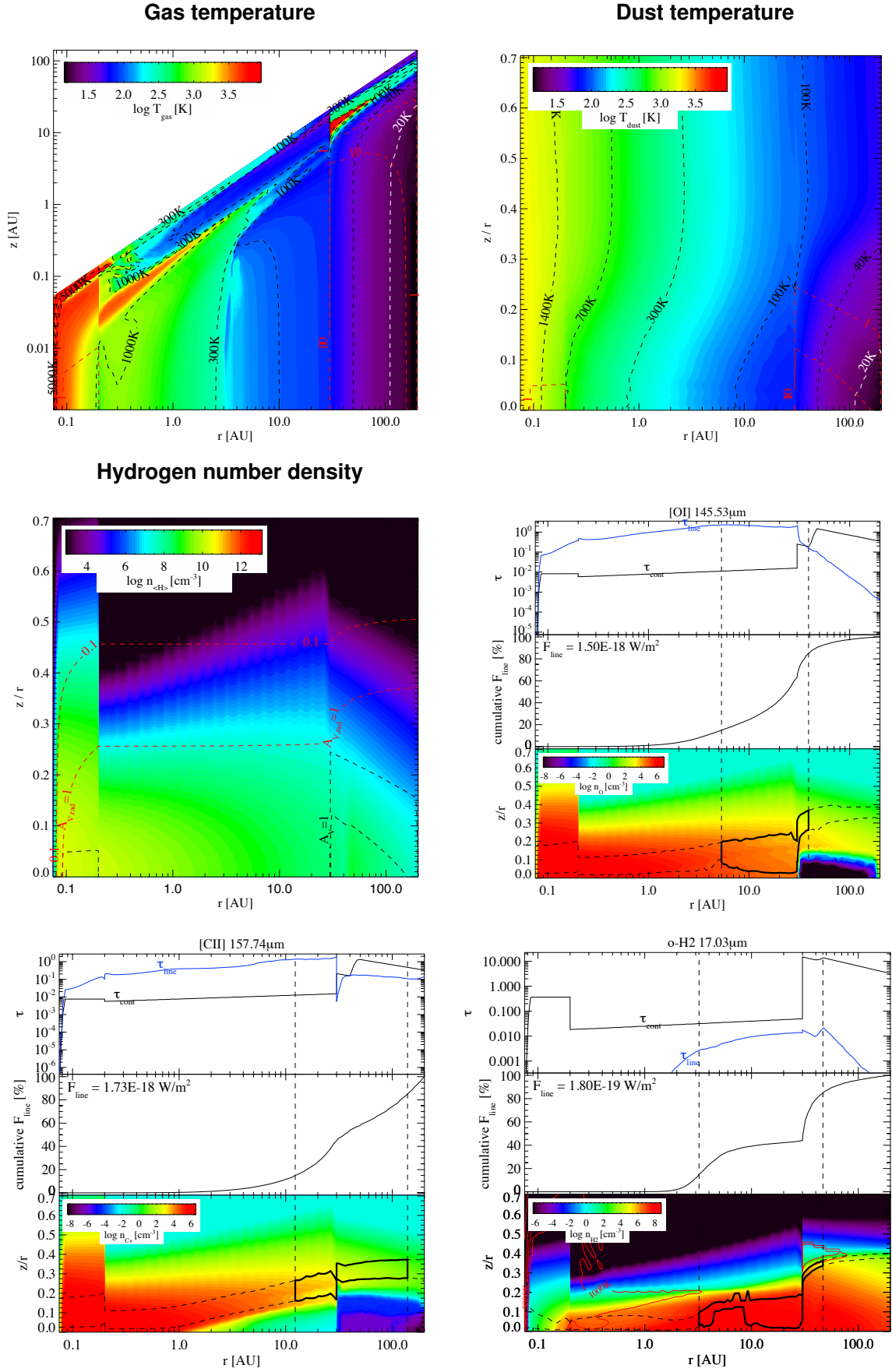


**Fig. A.4.** Model 5. *Upper panels:* (left) Gas temperature, (right) Dust temperature. *Central panels:* (left) Hydrogen number density, (right) optical depth of the line ( $\tau_{\text{line}}$ ), of the continuum ( $\tau_{\text{cont}}$ ), cumulative vertical flux, and number density as a function of the radius for the [O I] line at 145  $\mu\text{m}$ . The box in thick black lines represents the region in the disk that emits 70% of the line radially and 70% of the line vertically, thus approximately  $\sim 50\%$  of the line flux. *Lower Panels:* Similar plots for the [C II] line at 157  $\mu\text{m}$  (left) and the ortho H<sub>2</sub> 0-0 S(1) at 17  $\mu\text{m}$  (right).